Towards modeling wave-induced forces on an armour layer unit of rubble mound coastal revetments

Deping Cao[a], Jing Yuan[1a], Hao Chen[b]

[a] *Department of Civil and Environmental Engineering, National University of Singapore, 1 Engineering Dr. 2, Block E1A 07-03, Singapore 117576*
[b] *School of Engineering, University of Glasgow, Glasgow, UK*

Abstract

Wave-induced forces on an armour layer unit are key parameters for assessing the stability of rubble mound coastal revetment, but how to predict them accurately and efficiently remains an open question. This study explores the feasibility of using the Morison-type equation to convert numerically simulated porous media flow in an armour layer into the forces on a single armour unit. Wave flume tests are conducted, in which the forces on a cuboid placed in the armour layer of a sloped revetment were measured. In conjunction, numerical simulations were performed using an OpenFOAM solver, which treats the revetment as a porous media. The validated flow simulation was synchronized with the force measurement to illustrate the correlations between the predicted porous media flow and the impact force. Based on these correlations, a Morison-type predictor, which consists of inertial force, drag force, pressure gradient force and lift force, is proposed. The calibrated model can reasonably approximate the temporal variation of wave-induced force. However, it is found that the inertial coefficients vary significantly

[1] Corresponding author, Email: nusyuan@gmail.com

Preprint submitted to Ocean Engineering *August 10, 2021*

with the dynamic stability number and the initial submergence of the armour unit. Additional research is required to give a sufficiently large dataset for calibrating empirical formulae.
Keywords: Wave-induced force, Rubble mound revetment, Porous media, Armour layer stability, Numerical simulation

---

1. Introduction

Rubble mound revetments, due to their easy installation and good ability to dissipate wave energy, are widely used for shoreline protections around the world. Conventionally, an armour layer consisting of large pieces of rocks or artificial concrete units are placed on the seaward slope of a revetment to ensure the stability of the whole structure under extreme wave actions. Thus, quantifying the required size of an armour unit is a focal point of coastal-engineering research. In the past few decades, many experimental studies have been conducted to study the stability of armour layer under various wave conditions and revetment layout (e.g. Losada and Gimenez-Curto, 1979; Moghim and Tørum, 2012; van Gent, 2013; Herrera et al., 2017). There are also many similar studies on toe stability of revetment or breakwaters (e.g. Gerding, 1993; van Gent and van der Werf, 2014; Etemad-Shahidi et al., 2021). The stability number $N_s = H_s/(\Delta D_{n50})$ is introduced as an index of the stability of the armour layer, where H_s is the significant incident wave height at the toe of the structure; $\Delta = \gamma_s$ -1 with γ_s being the specific weight of armour layer material; and D_{n50} is the nominal median diamater or equivalent cube size of the armour unit. Another commonly used index, the dynamic stability number H_0T_0 (CIRIA, 2007), which combines the effects of both wave height and wave period, is defined as

$$H_0T_0 = N_s \times T_0 = H_sT_m/(\Delta D_{n50}) \times \sqrt{g/D_{n50}} \tag{1}$$

where g is the gravitational acceleration and T_m is the mean wave period.

Many formulae have been developed for assessing the stability of armour layer of rubble mound sloping structures. These formulae were mainly calibrated based on scaled model tests, in which the threshold value of a stability index, N_s, for a certain damage level was determined. For instance, the well-known Hudson formula (Hudson and Jackson, 1953) gives a no-damage (less than 5% of armour units are displaced) criteria for sloping rubble mound structure, which is applicable for both non-breaking and breaking waves on the foreshore. The Hudson formula can be extended for other damage level (e.g. Van der Meer, 1987), other layout of revetment, such a revetment with a berm (e.g. PIANC, 2003), and artificial armour units, such as tetrapod (e.g. van der Meer, 1988), X-bloc (e.g. DMC, 2003) and articulated concrete block mattress (ACB Mat) (e.g. Yamini et al., 2018, 2019).

Due to the complexity of wave interaction with armour layer, the uncertainty of the empirical stability formulae can be quite large, which is mainly due to the large scatter of the data used in model calibration. More importantly, these formulae must be used within the parameter space limited by the calibration dataset. Thus, they are often considered tools for preliminary design.

A process-based evaluation of armour layer stability must be built on quantitative knowledge on the wave-induced forces on an individual armour unit. However, the complexity of wave impacting a porous structure makes it very challenging to study the impact forces on an armour unit. Nevertheless, some flume experiments have been reported in the past few decades to shed some lights on this topic. Many of them attempted to examine if Morison-type equation, which consists of a drag force and an inertial force, can be used to link the measured force with the flow velocity close to the armour unit. Losada et al. (1988) measured the forces due to solitary waves attacking a single cubic block (not surrounded by other blocks) near a flat bottom. They proposed that the total force consists of a drag force, an inertial force and a lift force, and obtained the values of drag (C_D), inertial (C_I) and lift (C_L) coefficients by fitting the force measurements using flow velocity and acceleration estimated from solitary wave theory. Tørum (1994), in his flume experiments of periodic wave attacking a rubble mound revetment, measured the forces on a single rock unit in the armour layer and also sampled the nearby velocities. He then fit the Morison equation to the force components parallel and normal to the revetment surface, separately. He found that the normal force component cannot be described by the Morison equation. Cornett (1995) conducted a large set of flume experiments to investigate the spatial and temporal variation of impact force. He found that the peak horizontal force is maximized slightly below the still waterline, indicating that this is the most vulnerable region. The time history of the impact force strongly depends on the type of wave breaking on the slope. The strongest force under plunging breakers results from a sudden flow reversal under the steep wave crest. The largest force under surging breakers is caused by outward seepage flows that occur around the end of the run-down phase. Pramono (1997) studied the wave-induced forces on a cubical unit on submerged and low-crested breakwaters. He investigated the effect of the projected area of the armour unit on wave loading by changing the orientation of the unit. The wave loading was found to increase with increasing projected area of a unit. They also found that a rapid pressure gradient change can produce a shock pressure or impact on the armour unit. They set up a wave-induced force model by adding the pressure gradient induced force into Morison equation. Hofland (2005) studied the drag force acting on a single rock placed on a horizontal bed, and proposed to use the conventional quadratic law for estimating the drag force with a reference flow velocity at 0.15 times rock size above the bed. Although these studies have made solid contributions to revealing the wave loading on an armour unit, the problem remains largely open. A major concern is that the fitted coefficients (e.g., C_D, C_L, and C_I) have significant variations among these studies, which is partly because the reference flow velocity used in the Morison equation might be defined differently. For instance, some studies used the flow above the designated armour unit as the reference, which cannot represent the flow at the location of the unit.

Generally speaking, there are two groups of numerical work on the interaction between wave and a rubble mound structure in the published literatures. In the first group, the individual armour units are directly resolved. The typical numerical methods for this group are smoothed particle hydrodynamics (SPH) (Altomare et al., 2014) or combination of SPH and the discrete element method (DEM) (Ren et al., 2014; Sarfaraz and Pak, 2017, 2018). There are also some studies (Latham et al., 2009; Anastasaki et al., 2015; Xiang et al., 2019) that used combined finite and discrete element (FEMDEM) methods to model the wave-rock interaction in a rubble mound breakwater.

In the second group, the breakwater is generalized as a porous media, so the inividual armour units are not resolved. These models focused on predicting the flow behaviour. In these numerical models, Volume-averaged Reynolds-averaged Navier-Stokes (VARANS) equations were used to describe flows inside a porous media. For instance, del Jesus et al. (2012) developed the model IH-3VOF for simulating 3-dimensional wave-structure interaction based on VARANS equations and a volume-of-fluid (VOF) method for tracking free water surface. OpenFOAM, which is an open-source toolbox for the development of customized solvers, is becoming popular in the coastal engineering community, and a number of OpenFOAM solvers based on VARANS have been developed. Higuera et al. (2014) implemented the VARANS equations and a set of wave generation and absorption methods in OpenFOAM. Similarly, the VARANS equations proposed in Jensen et al. (2014) were also implemented in waves2foam toolbox developed by Jacobsen et al. (2012). When the momentum equation is volume averaged, two terms (frictional forces from the porous media and pressure forces from the individual grains) were modeled using Darcy-Forchheimer equation that includes two resistance coefficients which need to be determined. Higuera et al. (2014) tried different combinations of the two coefficients till the simulated results best fitted the measurements, while Jensen et al. (2014) proposed a method to determine the two coefficients which depends on the flow regime in the porous media. For the modeling the turbulence in the case of wave interaction with rubble mound structures, although different turblulece closure models were tested, i.e., Higuera et al. (2014) used both $k - \epsilon$ and SST $k - \omega$ models, Jensen et al. (2014) did not use turbulence model, acceptable agreements with experimental measurements were found in both papers. More recently, Larsen and Fuhrman (2018) proposed a new turbulence closure model, which demonstrated a better stability for a long duration of RANS simulation of surface waves.

The computational expense of the VARANS models is becoming affordable for practical applications due to the fast advancement of computational resources in recent years, so coastal engineers or researchers can use them as numerical wave tanks to obtain the flow characteristics within a porous coastal structure with a reasonable accuracy. The wave loading on a single armour unit is correlated with the volume-averaged flow at its location. If a Morison-type equation can be used to translate certain representative local flow parameters into the impact force, a 'short cut' will be established, which enables the VARANS-based models to evaluate the wave loading on a single armour unit. The aim of this paper is to explore if such a 'short cut' can be developed. Wave flume tests were conducted to obtain wave-induced forces on a single armour unit, and VARANS numerical simulations of the same flume tests provided the flow parameters. As such, a comprehensive dataset was established for relating the wave-induced forces on an armour unit with the volume-averaged flow parameters. We should point out that the same idea has been explored by some other researchers. For instance, Kobayashi and Otta (1987) used a numerical model that solves the depth-averaged flow on an impermeable slope and used Morison equation for assessing the impact force on an armour unit. Our work's advantage is that we use the state-of-the-art numerical model and direct measurements of impact force. The rest of the paper is arranged as follows. Section 2 describes the experiment setup and test conditions. Section 3 presents the numerical setup and validation. Surface flow over the revetment slope and wave-induced forces on a single armour unit are described in Section 4. Section 5 presents the set up of a Morison-type force predictor and the calibrated model coefficients. Finally, conclusions are given in Section 6.

2. Experiments

2.1. Experiment setup

Experiments were conducted in a wave flume in the Hydraulics Laboratory at National University of Singapore. This wave flume is 36 m-long, 1.3 m-deep and 2 m-wide. A piston-type wave maker supplied by HR Wallingford for generating waves is located at one end of the flume. A 1-on-3 sloped rubble mound revetment is installed near the other end of the flume. This revetment model follows the design of a new revetment in Singapore, which includes three layers, as illustrated in Fig. 1. A geometric scale of about 40 was used. The Froude number $F_r = U/\sqrt{gD_{n50}}$, where $U = \sqrt{gH}$), is maintained by geometric scaling. Following Tirindelli and Lamberti (2004), the viscous effect can be neglected when the Reynolds number $R_e > 10000 \sim 30000$ in the main flow. Yamini et al. (2018) also reported that viscous effect is negligible when $R_e > 2000$ in the armour layer. In the present study, an R_e, defined as $\sqrt{gH}D_{n50}/\nu$ (ν is the kinematic viscosity), is larger than 30000 in the main flow and larger than 2000 in the armour layer. The armour layer consists of gravels with mass = 40 to 100 g and $D_{n50} = 0.03$ m. The filter layer, which is between the armour layer and core, consists of gravels with mass = 2.4 to 4.8 g and $D_{n50} = 0.012$ m. The core layer consists of gravels with mass = 0.48 to 2.4 g and $D_{n50} = 0.007$ m. The model was installed with its toe at 24.89 m downstream of the wave maker. The toe is 0.36 m above the bottom of the flume. In front of the toe, there is a 3.2 m long foreshore with a slope $\approx$ 1:9. A vertical steel plate was installed at the onshore end of the rubble mound revetment to support the model and block water. Two photos of the revetment model are provided in Fig. 2.

In this study, the forces acting on a cuboid (made of Perspex) placed within the armour layer were measured. We chose to use a cuboid as an approximation of rock armour unit, because its geometry is well defined and it can be easily mounted onto a force sensor. The dimensions of the cuboid can also be changed (Fig. 3) to study the shape effect on wave loading. The cuboid was mounted to a three-axis force sensor, which was bolted onto a rigid bar sitting on top of the flume. There was a small gap between the cuboid and the surrounding rock armour units. This gap ensures that the cuboid will not touch any other objects during an experiment, so that the wave-induced force on the cuboid can be measured. Moreover, the water depth in the flume can be varied to investigate the effect of cuboid submergence.

2.2. Measurement instruments

The physical quantities measured in this study are: (a) free surface elevations in the flume, (b) the pore pressures in the core of the rubble mound revetment, (c) wave forces on the cuboid.

Five capacitance type wave gauges were installed to measure the surface elevations at a few selected locations. The gauges can measure a maximum wave height of 40 cm with an uncertainty of about 1 mm. Two wave gauges (named as CG1 and CG2) were installed at $X = 14.24$ and 14.8 m from the

Figure 1: Illustrative sketch of the revetment model and the location of measurement instruments (all dimension and distances are in [m]; not to scale).

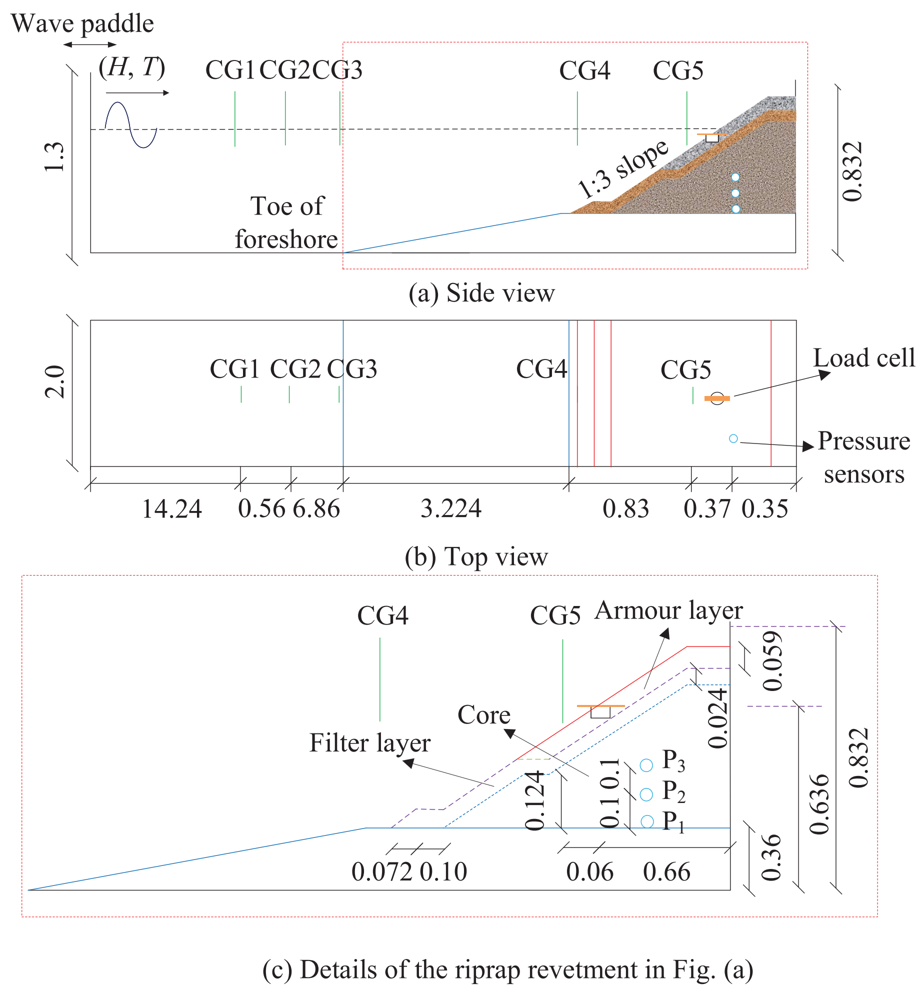

Figure 2: Photos of the rubble mound revetment and the experimental setup: (a) top view with sketch of the cuboid, load cell and the fixture; (b) side view

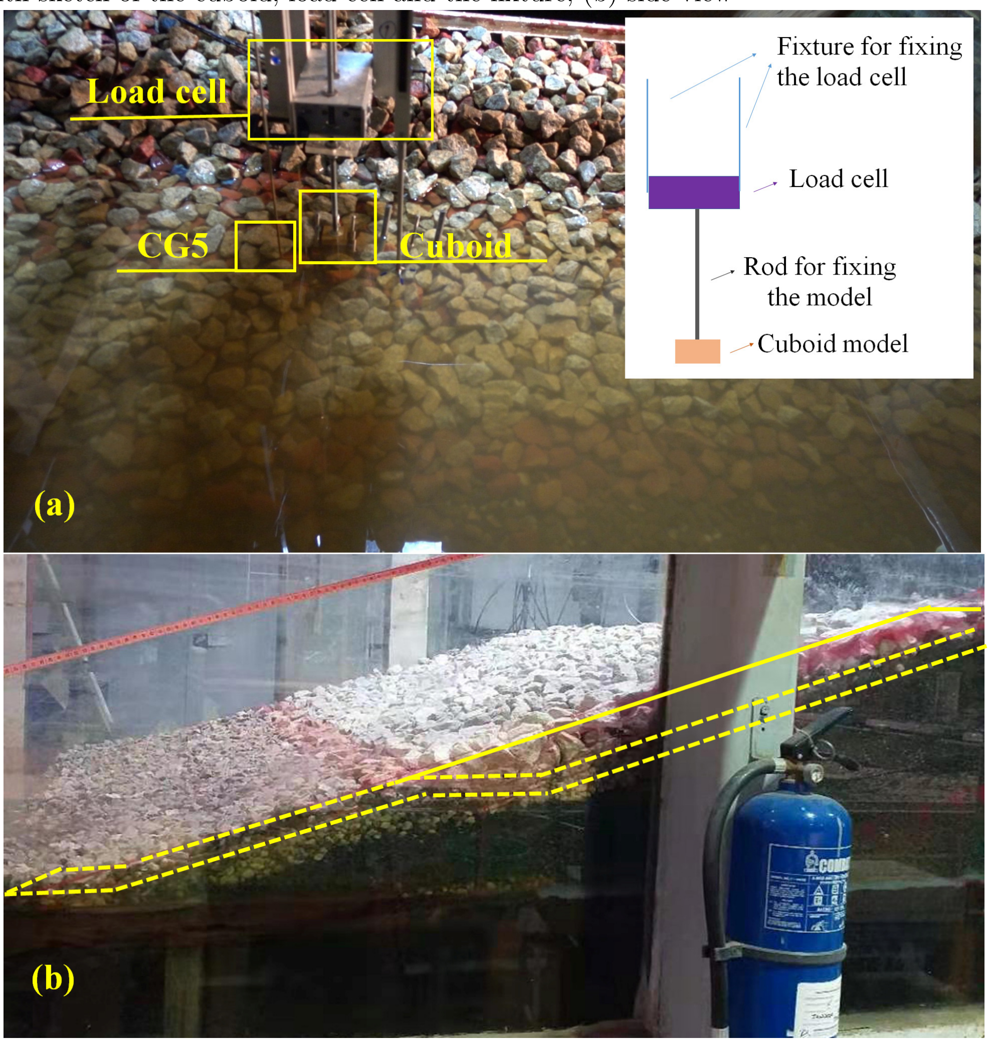

wave paddle for determining the incident and reflected waves through wave reflection analysis (see Section 3.4 for more details). The third and forth ones, CG3 and CG4, were installed slightly before the foreshore toe ($X = 21.66$ m) and the toe of rubble mound revetment ($X = 24.89$ m), respectively, for monitoring the wave condition right in front of the foreshore and that at the toe of the rubble mound revetment. Finally, a fifth wave gauge, CG5, was installed at $X = 25.72$ m to measure the surface elevation slightly before the cuboid.

Three pressure sensors (brand: STS 8370 Sirnach) with a measuring range of 0$\sim$50 mbar and measuring accuracy of $\pm$12.5 Pa were buried in the core layer (the detailed locations are shown in Fig. 1) for measuring the pore pressure changes. A Sony high-speed camera, with a sampling rate of up to 100 frame per second and a resolution of 1920 $\times$ 1080 pixels, was used to capture the process of wave-structure interaction. A three-component load cell (LSM-B-SA1, KYOWA) was deployed for measuring the force acting on the cuboid. This unit is a strain gauge based 3-component force transducer for simultaneously measuring force in 3 directions. It has a measuring capacity of 50 N and a natural frequency of 800 Hz. The measurement was sampled at a frequency of 200 Hz. A National Instrument (NI) data acquisition system was used to synchronize the signals of wave gauges and force sensor. The captured videos were synchronized with other instruments by identifying the moment when the flow touched the cuboid for the first time.

2.3. Test conditions

Totally 3 groups of tests were performed in this study. The first group (Group 1) tests various wave conditions (wave height H and wave period T)

for the same initial submergence (local water depth above the top surface of the cuboid, $h_l = 0.05$ m) and the same cuboid shape (height $h_m = 2$ cm, width $w_m = 4$ cm and length $l_m = 4$ cm).

The second group (Group 2) tests similar wave conditions and the same cuboid shape ($h_m = 2$ cm, $w_m = 4$ cm and $l_m = 4$ cm), but various initial submergence with $h_l = 0.01$ to 0.07 m or $h_l/D_{n50} = 0.31$ to 2.2. A very large initial submergence (e.g., $h_l/D_{n50} \approx \infty$) reduces the impact force to almost zero, since the surface wave no longer produces a strong flow around a deeply submerged armour unit. Also, a very large emergence (e.g., $h_l/D_{n50} \approx -\infty$) also gives a zero impact force, since the run-up flow can no longer reach the armour unit at a very high level. Thus, it can be expected that the impact force is maximized around the still water line. We also limit our study to positive initial submergence ($h_l/D_{n50} > 0$), so the armour unit is ensured to be fully submerged when the peak value of impact force occurs.

The third group (Group 3) tests the same wave conditions and the same initial submergence ($h_l = 0.05$ m), but various cuboid shapes. The configurations of the cuboid models used in the present study are shown in Fig. 3. D_{n50} of the cuboid in Fig. 3b and c are very close to that in Fig. 3a, but the projected areas in the parallel (denoted by ξ in Fig. 3a, which is equivalent to $//$) and normal directions (τ in Fig. 3a, which is equivalent to $\perp$) are changed, so the effect of projected area can be studied.

The details of the test conditions are listed in Table 1. Note that in the table, the Iribarren number is defined as $I_r = \tan\beta/\sqrt{H/L_0}$ and L_0 is the deep water wave length, $L_0 = gT^2/(2\pi)$. A larger I_r means that wave breaking is more surging and a smaller I_r means that the wave breaking is

Table 1: Experimental test conditions

Group No.	Test ID	h [m]	h_l [m]	H [m]	T [s]	I_r	H_0T_0	Cuboid dimensions [cm]
	A1			0.133	1.0	1.14	44.63	
	A2			0.132	1.2	1.38	53.15	
	A3			0.134	1.5	1.71	67.45	
	A4			0.134	1.8	2.05	80.94	
1	A5	0.686	0.050	0.054	2.0	3.58	36.24	4×4×2 (see Fig. 3a)
	A6			0.091	2.0	2.76	61.07	
	A7			0.109	2.0	2.52	73.15	
	A8			0.137	2.0	2.25	91.95	
	A9			0.163	2.0	2.05	109.4	
	B1	0.646	0.010	0.131		2.30	87.92	
2	B2	0.666	0.030	0.133	2	2.28	89.26	4×4×2 ((see Fig. 3a)
	B3	0.686	0.050	0.137		2.25	91.95	
	B4	0.706	0.070	0.138		2.24	92.62	
	C1						91.95	4×4×2 (see Fig. 3a)
3	C2	0.686	0.050	0.137	2	2.25	94.96	2×5×3 (see Fig. 3b)
	C3						94.96	5×2×3 (see Fig. 3c)

more plunging.

2.4. Data analysis

In the tests, most of the incoming wave energy is dissipated by wave breaking on the revetment slope and a small portion is reflected back to the wave paddle. Since our wave maker does not have the active wave-absorption function, the reflected waves are re-reflected by the wave maker towards the model, which is unrealistic and will contaminate the experiment results. Therefore, in the present study, only the experiment results before the leading re-reflected wave reaches the revetment are considered valid. The arrival times of the first mature wave and the first re-reflected wave at a given

Figure 3: Dimensions and orientation of the cuboid: (a) 4×4×2 cm cuboid; (b) 2×5×3 cm cuboid; (c) 5×2×3 cm cuboid.

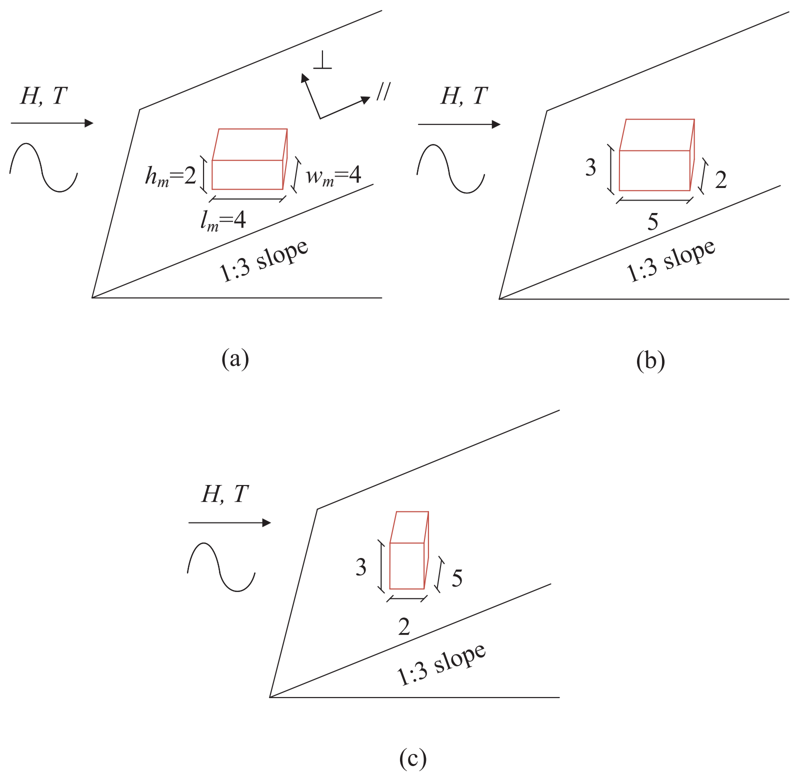

location in the flume were estimated using the wave celerity from linear-wave dispersion relation. The time window of valid measurements was defined by the two arrival times. Only the forces and the velocities within the time window were analysed. The free surface elevation measurements from the two neighboring wave gauges (CG1 an CG2) within the selected time window were then used for separation of incident and reflected waves using the method of Goda and Suzuki (1976). The obtained incident wave heights are listed in Table 1. The measured wave reflection coefficient (=ratio of reflected and incident wave height) is about 0.4∼10% for $I_r = 1.14{\sim}3.58$, which is smaller than those of similar rubble mound breakwater as reported in Díaz-Carrasco et al. (2021) and those of ACB Mat as reported in Yamini et al. (2019). This indicates that the energy of the incident waves was mostly dissipated and absorbed by the porous rubble mound revetment in the present study and wave reflection is very small.

The dry weight of the cuboid (about 0.37 N for the Perspex armour unit in Fig. 3a) was first subtracted from the vertical component of force measurement. Since we are interested in the force components normal ($F_\perp$) and parallel ($F_{//}$) to the slope, the measured force components in the horizontal and the vertical directions are projected onto the slope-parallel and slope-normal directions. The force measurements contained some high-frequency noises, so the raw measurements were filtered using a low-pass filter with a cut-off frequency of 10 Hz. Fig. 4 show the processed data of an example case $h0.706H0.15T2.0$ ($h = 0.706$ m, $H = 0.15$ m, $T = 2.0$ s), including surface elevations (Figs. 4a and b), dynamic pore water pressures (with hydrostatic pressure subtracted and that the dynamic pore pressures are normalized by dividing ρg, Fig. 4c) and force components (Fig. 4d). Because the buoyancy was included in the vertical component of force measurement in Fig. 4d, $F_\perp$ is always positive. Since the armour unit is mostly submerged in the water, buoyancy (about 0.32 N for the armour unit in Fig. 3a) is deducted from the total force. By doing so, the dynamic part of the total force is better presented, which will be the focus of the following context and simply refered to as the 'force'.

3. Numerical simulation

A number of openFOAM solvers based on VARANS equation are available, e.g. IHFOAM (e.g. del Jesus et al., 2012), waves2Foam (e.g. Jensen et al., 2014) and olaFlow (e.g. Higuera, 2015). Here we choose the olaFlow in this study, but our findings can be applied to other solvers of the same type.

3.1. Governing equations

The model was based on Volume-averaged Navier-Stokes equations for two-phase flow. Readers are referred to Higuera (2015) for more details. Here the governing equations are reproduced below.

$$\frac{\partial}{\partial x_i} u_i = 0 \tag{2}$$

$$\begin{aligned}(1+c)\frac{1}{n}\frac{\partial(\rho u_i)}{\partial t} + \frac{1}{n}\frac{\partial}{\partial x_j}\left(\frac{\rho u_i u_j}{n}\right) = -\frac{\partial p^*}{\partial x_i} - g_j x_j \frac{\partial \rho}{\partial x_i} + \\ \frac{1}{n}\frac{\partial}{\partial x_j}(\mu+\mu_t)\left(\frac{\partial u_i}{\partial x_j} + \frac{\partial u_j}{\partial x_i}\right) - A u_i - B\rho\sqrt{u_j u_j}\, u_i\end{aligned} \tag{3}$$

$$\frac{\partial \alpha_1}{\partial t} + \frac{1}{n}\frac{\partial u_i \alpha_1}{\partial x_i} + \frac{1}{n}\frac{\partial}{\partial x_i}(u_i^r \alpha_1(1-\alpha_1)) = 0. \tag{4}$$

Figure 4: An example of: (a) measured surface elevations CG1; and (b) CG5; (c) measured pore pressures P_1 to P_3; (d) the force components parallel and normal to the revetment slope ($h0.706H0.15T2.0$, $t = 0$ in this figure is the beginning of data acquisition.)

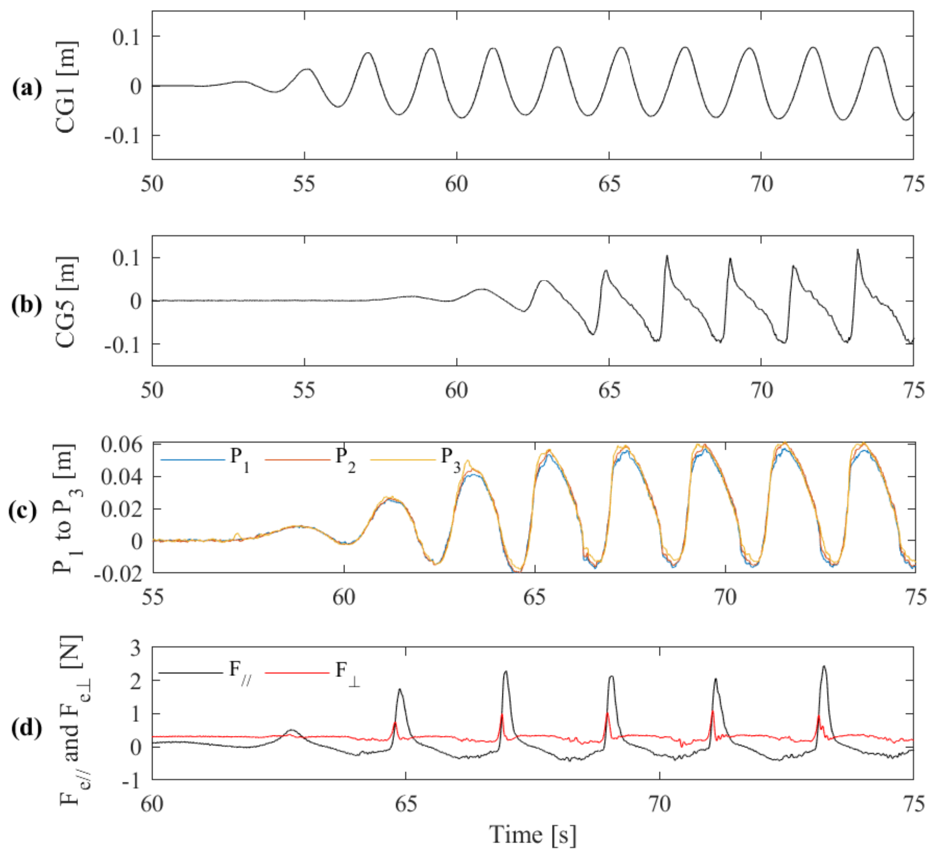

where u_i and u_j are the volume-averaged velocities in Cartesian coordinates; u^r is the relative velocity between fluid and air; x_i and x_j are the Cartesian coordinates; n is the porosity ($n = 1$ for water); ρ is the fluid density; p^* is the pseudo-dynamic pressure; g is the gravitational acceleration; μ is the dynamic molecular viscosity of fluid and μ_t is the dynamic turbulent viscosity of fluid; α_1 is the volume of fluid (VOF) indicator function; c is the coefficient for added mass; A and B are two model coefficients.

Any property of the fluid in each cell is calculated by weighting them by the VOF function. For example, density of the fluid in a cell ρ is computed as,

$$\rho = \alpha_1 \rho_w + (1 - \alpha_1)\rho_a \tag{5}$$

where ρ_w and ρ_a are the densities of water and air phase.

According to some previous studies (del Jesus et al., 2012; Higuera et al., 2014; Higuera, 2015), $c = 0.34$ is recommended. A and B are defined as,

$$A = \alpha \frac{(1-n)^3}{n^3} \frac{\mu}{D_{n50}^2} \tag{6}$$

$$B = \beta(1 + \frac{7.5}{KC}) \frac{1-n}{n^3} \frac{\rho}{D_{n50}} \tag{7}$$

where α and β are two model coefficients that can be tunned by the user and KC is the Keulegan-Carpenter number, which is defined as,

$$KC = \frac{U_M T}{n D_{n50}} \tag{8}$$

In Eq. (8), U_M is the maximum oscillatory velocity and T is the period of the oscillation.

In the present study, the turbulence is mostly generated at the moment of wave breaking on the slope of the revetment. Here we chose SST $k-\omega$ model

Table 2: Parameters used in the numerical simulation

Material	D_{n50} [m]	Porosity n	α	β
armour layer	0.03	0.45	50	0.6
Filter layer	0.012	0.43	50	2.0
Core	0.007	0.35	50	1.2

(one of the turbulence models provided in OpenFOAM) as the turbulence closure model. We noticed that there are many other turbulence closure models, among which the modified turbulence model by Larsen and Fuhrman (2018) is able to avoid the unphysical growth of eddy viscosity and inevitable wave decay. This modification is important for a long duration of simulation (more than 40∼50 wave cycles), e.g., Fig. 4 of Larsen and Fuhrman (2018). In the present study, we only simulated less than 32 wave cycles to obtain a periodic result. Therefore, we chose SST $k-\omega$ turbulence model for the simplicity of use in OpenFOAM. We also noted that the simulated results would not be significantly affected even without using a turbulence closure model, which is possibly because the turbulence terms are much smaller than the drag and inertia terms in the porous zone.

The wave was generated on the left patch with active absorption. The solver olaFlow in OpenFOAM was used to solve the VARANS equations. The specific physical properties of the porous media are given in Table 2. Note that the default values of α and β as proposed in Higuera (2015) are used.

The numerical model predicts volume-average flow and pressure gradient at the location corresponding to the centroid of an artificial armour unit, which will be used in the force predictor in Section 5.1.

Figure 5: Computational domain and mesh (unit: [m]; not to scale; red cross denotes the artificial cuboid)

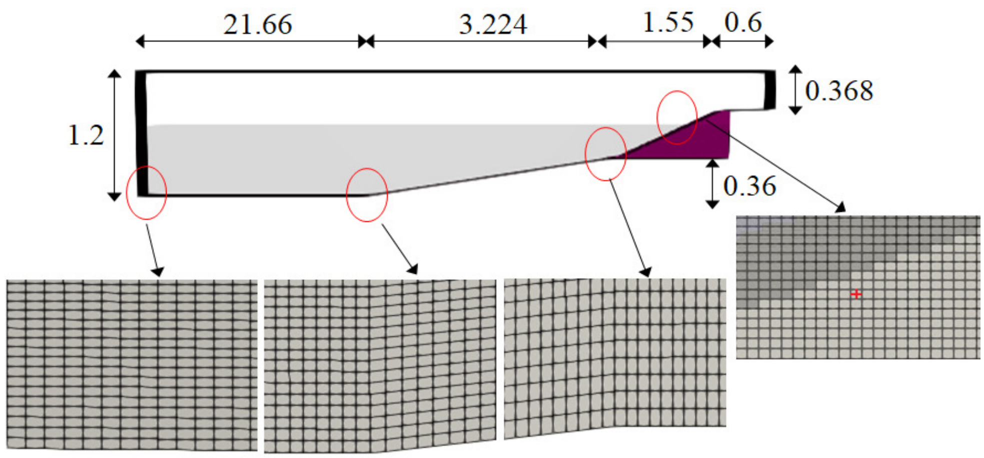

337 *3.2. Computational domain and mesh*

338 A 2D numerical model was set up to reproduce the above experiments. 339 The domain, as shown in Fig. 5, has a length of 21.66 m from the left inlet 340 to the toe of foreshore, 3.224 m long foreshore and 1.55 m long revetment. 341 The heights of the revetment and the whole domain are 0.832 m and 1.2 m, 342 respectively. The rubble mound revetment was modeled as a porous media 343 consisting of three different layers with different porosity n and D_{n50}.

344 The whole domain consists of three sections, i.e., the wave maker region, 345 the foreshore region and the revetment region. The cell size in the revetment 346 region is the smallest, and is about 1/3 of that in the wave making region. 347 The artificial cuboid centroid is marked with a red cross in Fig. 5. Since the 348 cuboid is much larger than the cell size, the simulated flow at the cuboid 349 centroid is extracted from a cell inside the porous media, so this flow is a 350 porous media flow.

3.3. Convergence study

Four types of grids with different cell sizes have been tested for the case $h0.686H0.06T2.0$, as shown in the Table 3. The comparisons of surface elevations at CG1 and CG5 are shown in Fig. 6. It can be seen that the results generally resemble each other. To show the convergence, the root-mean-squre error (RMSE) for i-th grid (i = 1, 2, 3, 4) compared to Grid 4 is first calculated and then normallized by RMS of Grid 4, for CG1 and 5, respectively. As shown in Table 3, the RMSE (in percentage) of CG1 and CG5 reduces as grid becomes finer and is less than 5% for Grid 3, which can be considered negligible. Hence, Grid 3 is applied for all the simulations used in the following discussions.

Table 3: Mesh parameters for the convergence study and RMSE normalized by RMS of CG1 and CG5 based on Grid 4 for each grid size. The cell size is the averaged size at the free surface area, as there is a smooth refinement from the far end near the wave-maker boundary to the area near the revetment.

Grid No.	Wave-making region		Foreshore region		revetment region		Mesh No.	RMSE [%]	
	$\Delta x[cm]$	$\Delta z[cm]$	$\Delta x[cm]$	$\Delta z[cm]$	$\Delta x[cm]$	$\Delta z[cm]$	[million]	CG1	CG5
1	3.09	0.80	1.61	0.69	0.75	0.62	0.15	9.9	20.4
2	2.58	0.66	1.34	0.58	0.63	0.51	0.21	2.9	5.6
3	2.06	0.53	1.07	0.46	0.50	0.41	0.33	2.0	2.8
4	1.55	0.40	0.80	0.35	0.38	0.31	0.58	-	-

3.4. Validation

The simulation and the measurement are synchronized by matching simulated and measured CG5 time series. More specifically, we took out a piece of CG5 measurement, which has 2∼3 periodic cycles, and matched it with

Figure 6: Convergence tests for the numerical model (see Table 3 for grid resolutions): (a) CG1, (b) CG5. The simulation is for the case $h0.686H0.06T2.0$.

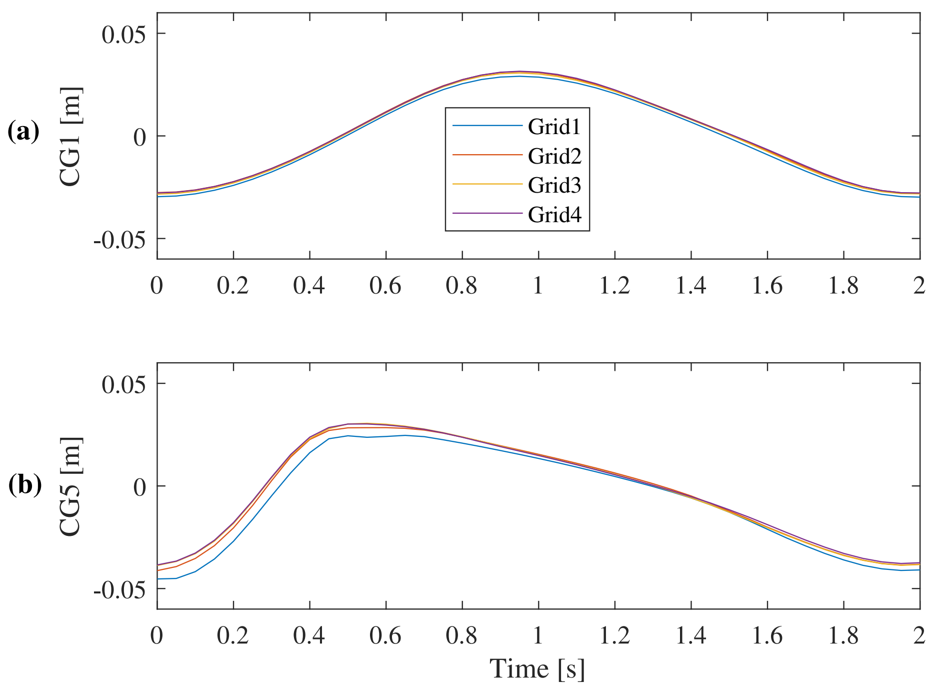

the last 2∼3 cycles of the simulated surface level at CG5, which is also very periodic. The time coordinate of the measurement was adjusted until the two time series were best matched. Subsequently, $t = 0$ is defined as the beginning of the two synchronized time series of CG5. Since all instruments were synchronized, the time coordinates of other measurements were also adjusted. Note that the $t = 0$ does not have any physical meaning, since the beginning of the selected piece of CG5 measurement was rather arbitrarily chosen (but $t = 0$ is around the time of negative peak value of CG5). Fig. 7 shows the comparison of simulated and measured surface elevations (CG1 and CG5 as an example) and dynamic pore pressures (P_1 and P_3 as an example) for two selected cases, i.e., the left and right panels are for the case $h0.686H0.06T2.0$ (relatively larger wave period and smaller wave height) and $h0.686H0.15T1.2$ (relatively smaller wave period and larger wave height), respectively. As will be introduced later, the first case has a larger $I_r = 3.58$, so a surging-type breaker occurred and the green-water run-up flow was observed. The second case has a much smaller $I_r = 1.38$, so a plunging-type breaker occurred, which created a very turbulent run-up bore on the slope.

As shown in Fig. 7a, the simulated and measured time histories of the surface elevations by CG1 agree well with each other for both cases, with a discrepancy of the peak value of less than 8%. CG5 measures the surface elevation right in front of the cuboid. After shoaling and wave reflection by the porous revetment, the time history of the surface elevation at CG5 in Fig. 7b is very different from that measured by CG1, which has been well simulated by the numerical model. Waves can induce the pressure fluctuations in the pores of the porous revetment. The time histories of the simulated dynamic

Figure 7: Model validation: (a) CG1; (b) CG5; (c) P_1; (d) P_3 for two cases $h0.686H0.06T2.0$ (left panel) and $h0.686H0.15T1.2$ (right panel)

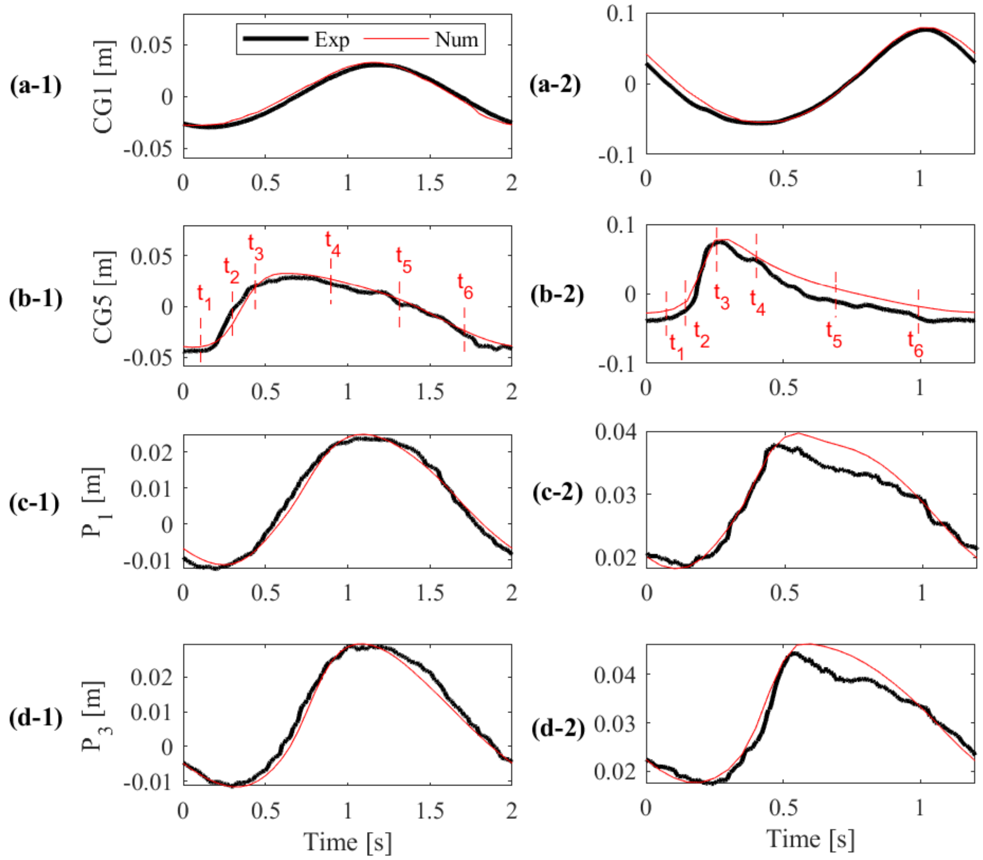

pore pressures (P_1 and P_3) in Fig. 7c and d are almost the same as the measured ones for the case $h0.686H0.06T2.0$. For the case $h0.686H0.15T1.2$, the peak values of P_1 and P_3 are slightly underestimated by about 5%. In Fig. 7b, six moments of CG5 are marked in both cases (t_1 to t_6) for later discussions on flows and forces.

4. Surface flows over the revetment slope and wave-induced forces on a single unit

4.1. Surface flows over the revetment slope

Since the numerical model has been well validated against the experimental measurements, here we can discuss the flow process mostly based on the numerical results. Fig. 8 presents six key moments (corresponding to t_1 to t_6 indicated Fig. 7b-1) of wave run-up and run-down along the revetment slope for the case with a large Iribarren number ($I_r = 3.59$), $h0.686H0.06T2.0$. The case $h0.686H0.15T1.2$ which has a small $I_r = 1.38$ is presented in Fig. 9. The selected six moments are marked as t_1 to t_6 in Fig. 7b-2. In both Figs. 8 and 9, the initial still water lines, the artificial cuboid (not included in the simulation) and the measuring instruments are also shown for easy interpretation of the findings. More attention is given to the flow characteristics in the area around the cuboid in the following discussion.

For the case with a large I_r in Fig. 8 (surging breaker): At moment t_1 (Fig. 8b-1), the incoming wave is about to reach the revetment and break. The water depth near the cuboid (e.g., measured by CG5) is around the lowest level and the cuboid is covered by a thin layer of water. The velocity vectors show that water under the arriving wave is flowing onshore or towards the revetment. The falling water table inside the revetment is still higher than the free surface above the cuboid, which drives an offshore internal flow and a run-down flow along the revetment surface. At the point where the two main flows meet each other, a strong upward seepage flow is created (highlighted by the yellow dashed box). The exit point of outward seepage on the slope (denoted by the star) is moving upslope towards the cuboid.

Figure 8: The key moments of wave-revetment interaction for the case $h0.686H0.06T2.0$ ($I_r = 3.59$): the snapshots from the camera recordings in (a-1) to (a-6) and the simulated results in (b-1) to (b-6) correspond to t_1 to t_6 indicated in Fig. 7b-1. The yellow solid lines in Fig. 8b denotes the initial still water line. The yellow star denotes the exit point of outward seepage. The yellow and green circles represent the location of the artificial cuboid and the three pressure sensors, respectively.

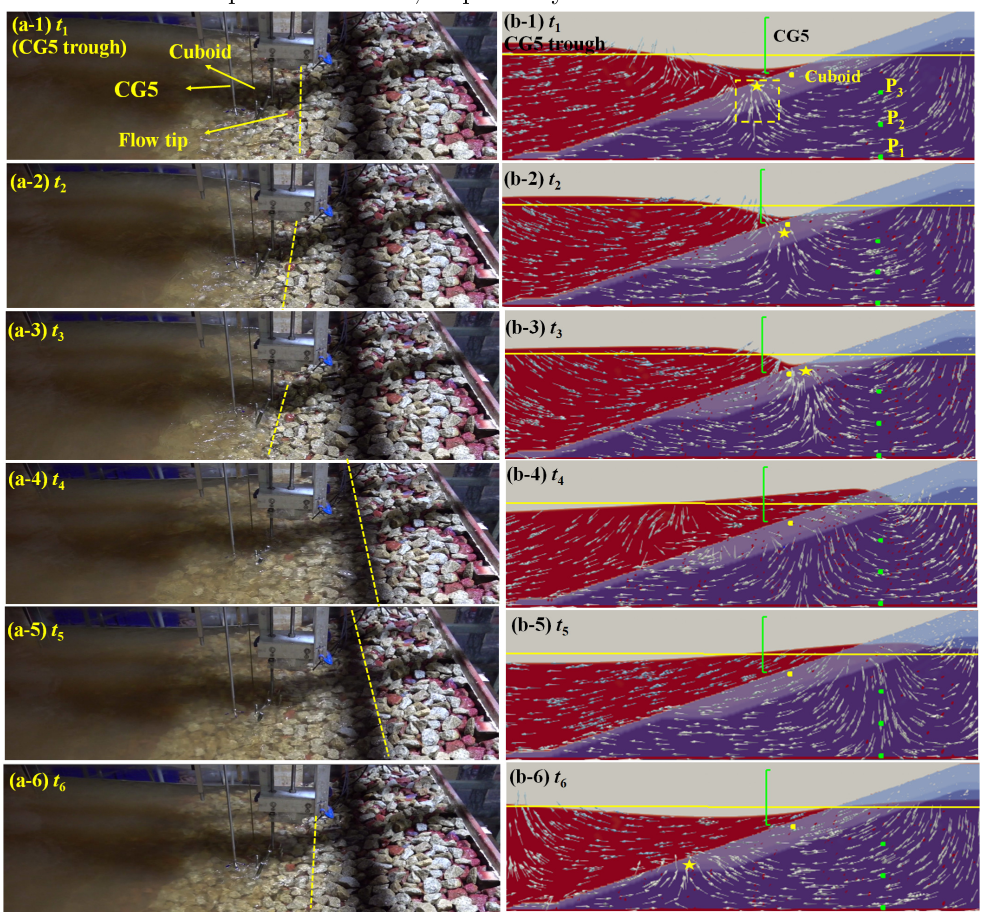

Figure 9: The key moments of wave-revetment interaction for the case $h0.686H0.15T1.2$ ($I_r = 1.38$): the snapshots from the camera recordings in (a-1) to (a-6) and the simulated results in (b-1) to (b-6) correspond to t_1 to t_6 indicated in Fig. 7b-2. The yellow solid lines in Fig. 9b denotes the initial still water line. The yellow star denotes the exit point of outward seepage. The yellow and green circles represent the location of the artificial cuboid and the three pressure sensors, respectively.

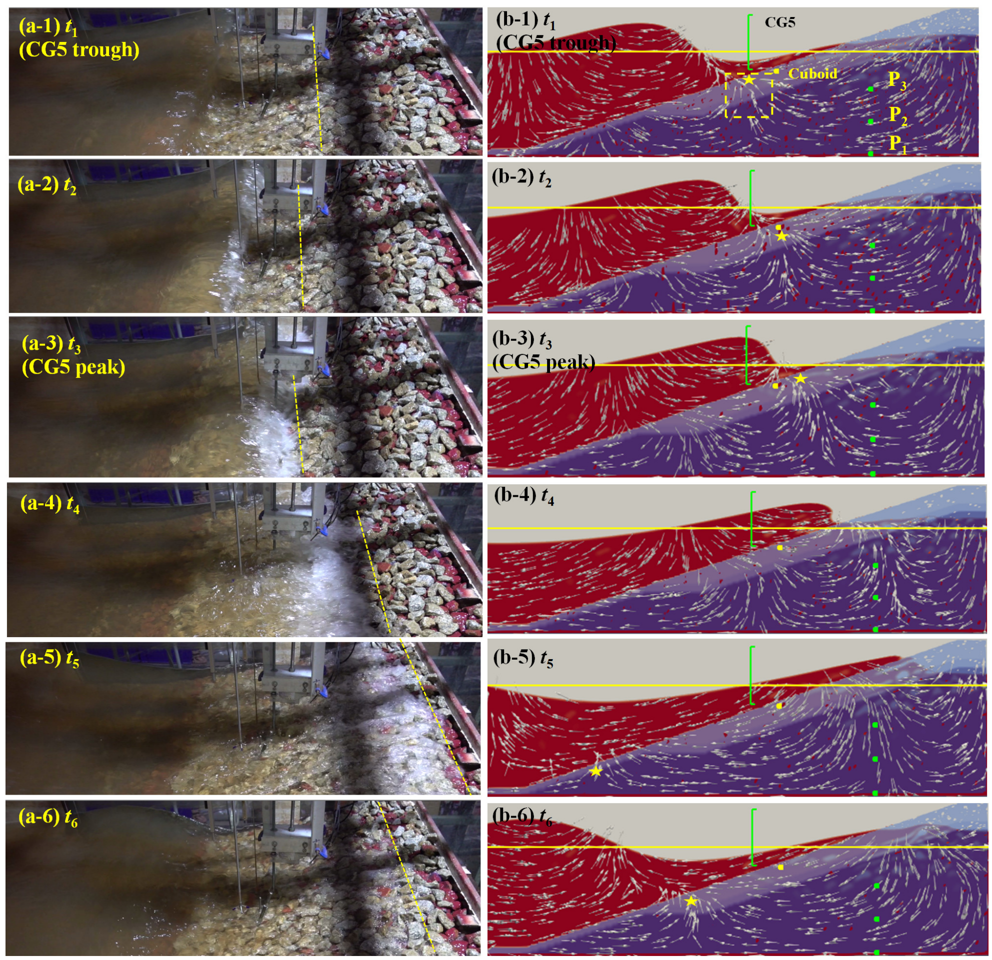

At moment t_2 (Fig. 8b-2), the run-down flow on the revetment slope continues and the exit point of outward seepage reaches the cuboid's location. This is actually when the maximum $F_{\perp}$ occurs, as will be shown later.

At moment t_3 (Fig. 8b-3), the run-down flow on the revetment slope is about to stop. The main body of run-up flow produced by a surging breaker arrives at the cuboid, where the direction of slope-parallel velocity is suddenly changed from downward to upward ('flow reversal'), leading to a large up-slope acceleration. This is the moment when the maximum $F_{//}$ occurs, as will be seen later in Fig. 10a. Water starts to run up the slope and flow into the porous revetment. As a result, the water table inside the revetment begins to rise.

At moment t_4 (Fig. 8b-4), the main body of run-up flow has passed the cuboid location, and the cuboid becomes increasingly submerged. Water also flows into the revetment across the armour layer, causing the internal water table to rise. It is also noted that the flow above the toe of revetment is already reversed to go offshore.

The maximum run-up occurs between t_4 and t_5, so at the moments t_5 and t_6 (shown in Fig. 8b-5 and b-6), run-down flow develops on the revetment slope. The flow around the cuboid during the run-down stage is mostly parallel to the slope and the velocity gradually increases. The cuboid experiences a downslope force.

For the case with a small I_r in Fig. 9 (plunging breaker), some observations similar to those in Fig. 8 (surging breaker) can be made. When the incoming wave arrives at the revetment, it meets the run-down flow and the internal offshore-directed porous media flow produced by the previous wave, leading to an outward seepage flow along the line where the two major flows converge. The exit of the outward seepage flow moves upslope subsequently, so there is a moment (Fig. 9b-2) when the cuboid experiences a strong outward flow, which leads to the peak of out-of-slope $F_{\perp}$. The plunging breaker creates a run-up bore with a highly aerated and almost vertical front (Fig. 9a-2 to a-4, b-2 to b-4), which is different from the 'peaceful' bore produced by a surging breaker. When the main body of the bore passes the cuboid (Fig. 9b-3), the local flow is quickly reversed from down-slope to up-slope, so a strong upslope flow acceleration is produced, which eventually gives the peak of upslope $F_{//}$. The turbulent and almost vertical front of the bore makes the flow reversal more 'sudden' than that in the surging-breaker case.

4.2. Wave-induced force on a single armour unit

The time history of the wave-induced force can be related to the flow behavior around the cuboid discussed in the previous section. Figs. 10 and 11 show the measured force on the cuboid together with some flow parameters for the two cases shown in Figs. 8 and 9, respectively. Here the flow parameters include the simulated velocity and acceleration at the cuboid's centroid, which are later used as the input parameters for predicting the wave-induced forces. The water surface and above the cuboid's centroid (simulated) are also presented. The two representative cases have some common characteristics of the temporal variations of wave-induced forces. First, the peak values of $F_{//}$ are larger than those of $F_{\perp}$, which is also applicable for the rest of cases in this study. This is understandable, because the main flow is parallel to the slope and seepage flow is secondary. Second, the positive

Figure 10: Measured force and simulated flow conditions for case $h0.686H0.06T2.0$ (t_1 to t_6 are the moments shown in Fig. 8): (a) measured wave induced force, (b) and (c) simulated flow acceleration and velocity at the centroid of the cuboid, (d) simulated surface elevation at the x-location of the cuboid (η=0 is initial water level.)

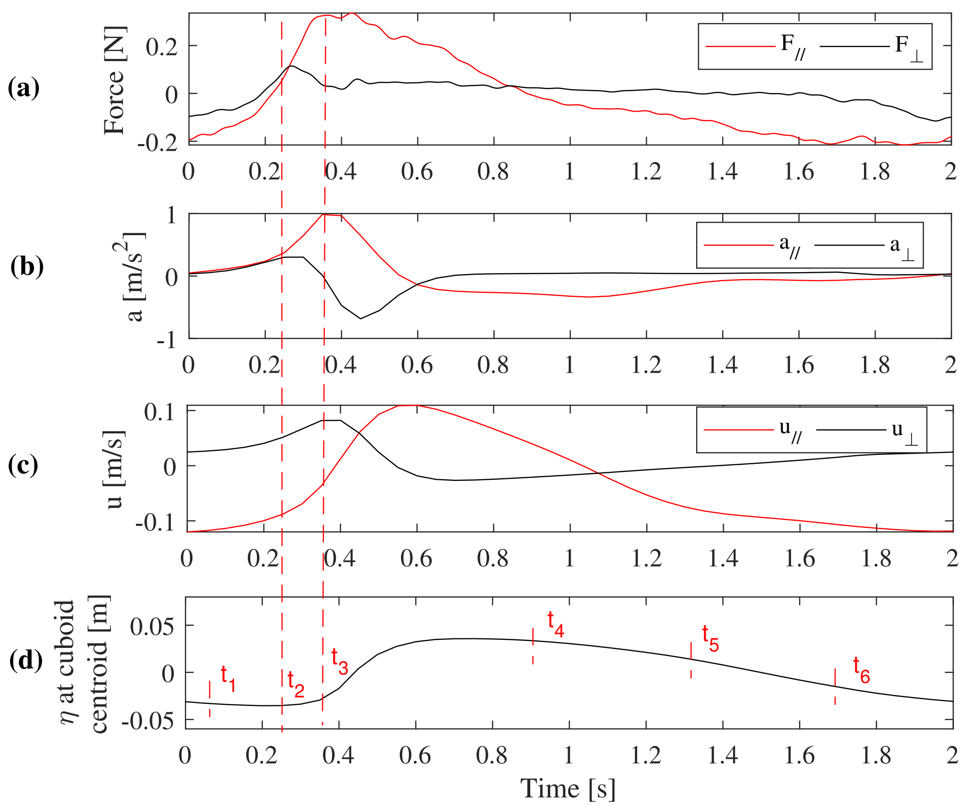

Figure 11: Measured force and simulated flow conditions for case $h0.686H0.15T1.2$ (t_1 to t_6 are the moments shown in Fig. 9): (a) measured wave induced force, (b) and (c) simulated flow acceleration and velocity at the centroid of the cuboid, (d) simulated surface elevation at the x-location of the cuboid (η=0 is initial water level).

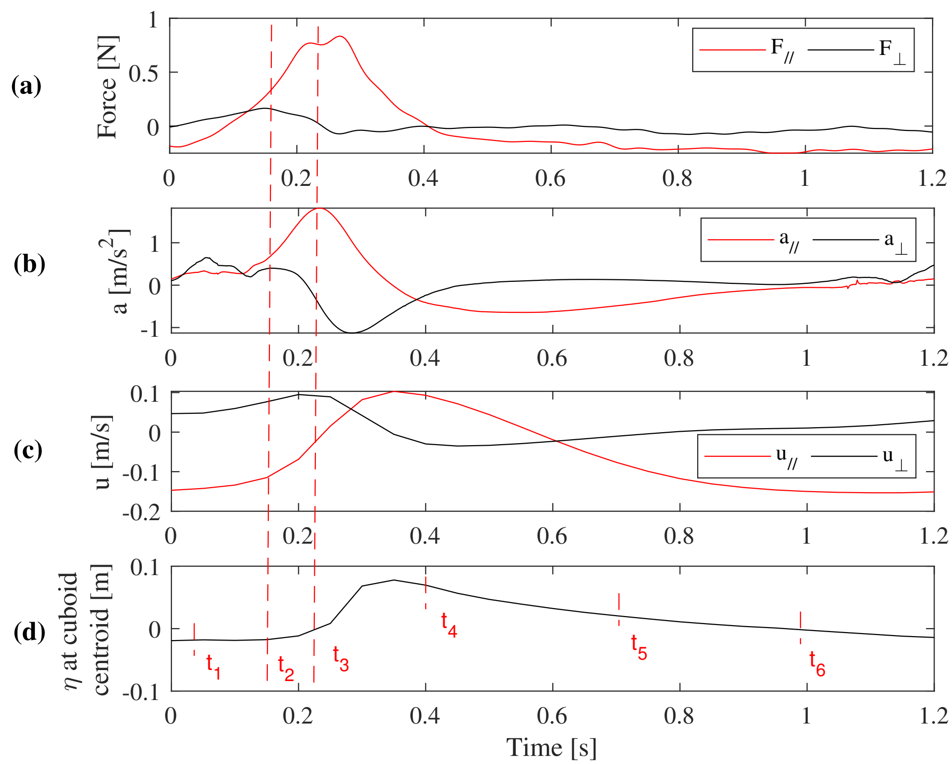

peak of $F_{//}$ occurs when the flow at the cuboid reverses from run-down to run-up, which gives the peak value of slope-parallel acceleration $a_{//}$. This is consistent with the finding of Cornett (1995) who found that the largest forces parallel to the slope are caused by the sudden flow reversal. Third, the positive peak of $F_{\perp}$ occurs slightly earlier than $F_{//}$, when the exit of outward seepage flow is located around the cuboid's location. For the larger I_r case in Fig. 10, the global positive and negative peaks in a wave cycle have comparable magnitudes for both $F_{//}$ and $F_{\perp}$, while for the smaller I_r case in Fig. 11, the positive peak of $F_{//}$ has a much larger magnitude than the negative peak of $F_{//}$.

As reviewed in the introduction, the dynamic stability number, H_0T_0 combines the effects of wave period and wave height and it is closely related to damage of the rubble mound revetment (CIRIA, 2007). Stability of the armour layer is closely related to the peak forces on a single armour unit, so it can be expected that the peak values of the impact force are also correlated to H_0T_0. To this end, we plot the positive peak values of $F_{//}/\Delta\rho g D_{n50}^3$ and $F_{\perp}/\Delta\rho g D_{n50}^3$ against H_0T_0 in Fig. 12 for Group 1 cases. Note that in the present study, only regular waves are studied. H_s and T_m are replaced by H and T, respectively in Eq. (1). Fig. 12 clearly shows that as H_0T_0 increases from 36 to 109, both $F_{//}/\Delta\rho g D_{n50}^3$ and $F_{\perp}/\Delta\rho g D_{n50}^3$ increase monotonically. The initial submergence of the cuboid h_l/D_{n50} is another important parameter that may affect wave-induced forces on the cuboid. Group 2 tests of this study aim at investigating the change of impact force for h_l/D_{n50} from 0.31 to 2.2. Figs. 13a to d present the measured forces for Group 2 tests. Note that these tests have the same wave conditions. Generally speaking, the time

Figure 12: Positive peaks of force components versus H_0T_0 for Group 1 cases

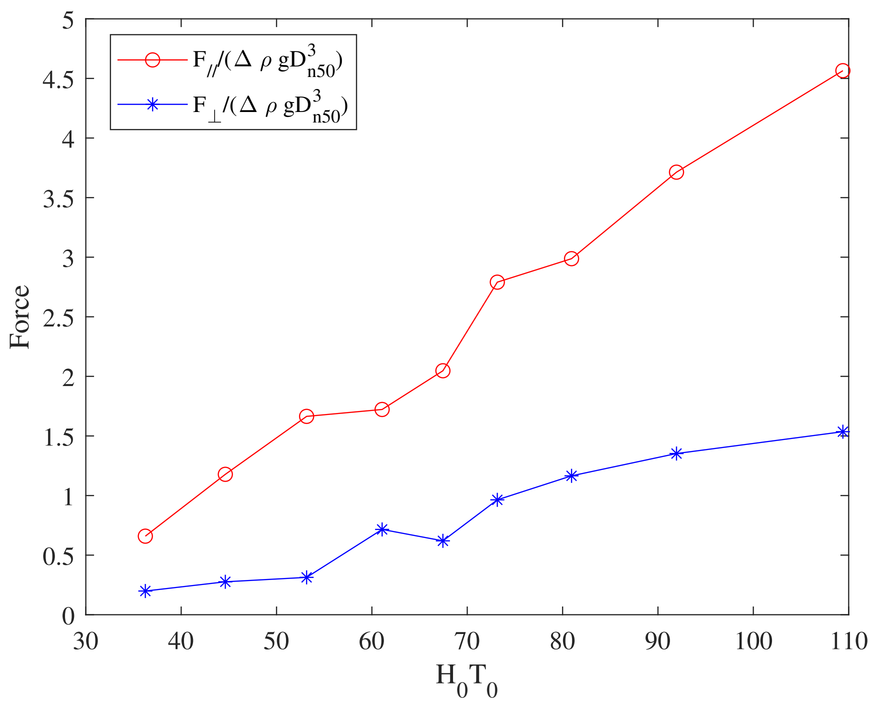

series of $F_{//}$ at various h_l/D_{n50} are similar. The positive peaks have similar magnitudes (about 2 N). Among the four tests, three of them have a single positive peak of $F_{//}$, while only the test with the lowest h_l/D_{n50} (Fig. 13a) shows two positive peaks. This is possibly because the cuboid in this test is not fully submerged when the run-up flow arrives. The time series of $F_\perp$ also have similar characteristics. Among the four tests, the poitive peak of $F_\perp$ occurs slightly before the positive peak of $F_{//}$, and its magntude is more-or-less the same (about 0.7 N). Overall speaking, the variation of peak forces of $F_{//}$ and $F_\perp$ for various h_l/D_{n50} are small, i.e., $F_{//} = 2.14$ N ($\pm 7\%$) and $F_\perp = 0.74$ N ($\pm 15\%$), suggesting that the rock units within a belt between $h_l/D_{n50} = 0.31$ to 2.2 below the water line are equally vulnerable.

5. Force predictor

In the present study, our goal is to explore if the Morison-type equation can be used to predict the wave-induced force on a single armour unit located near the still water line on a sloped revetment. The model is expected to take the predicted flow parameters at the centroid of the armour unit as model inputs, and yields time series of 2-dimensional impact force as model outputs. The setup of the model is introduced first, followed by model calibration and model validation.

5.1. Setup of the model

Here we consider 2-dimensional problems, so an armour unit experiences a parallel force $F_{//}$ (parallel to slope) and a normal force $F_\perp$ (perpendicular to slope), i.e.,

$$\overrightarrow{F} = (F_{//}, F_\perp) \tag{9}$$

Figure 13: Figures showing time series of forces for Group 2 tests, which have different initial submergence: (a) $h_l/D_{n50} = 0.31$; (b) $h_l/D_{n50} = 0.94$; (c) $h_l/D_{n50} = 1.57$; (d) $h_l/D_{n50} = 2.2$.

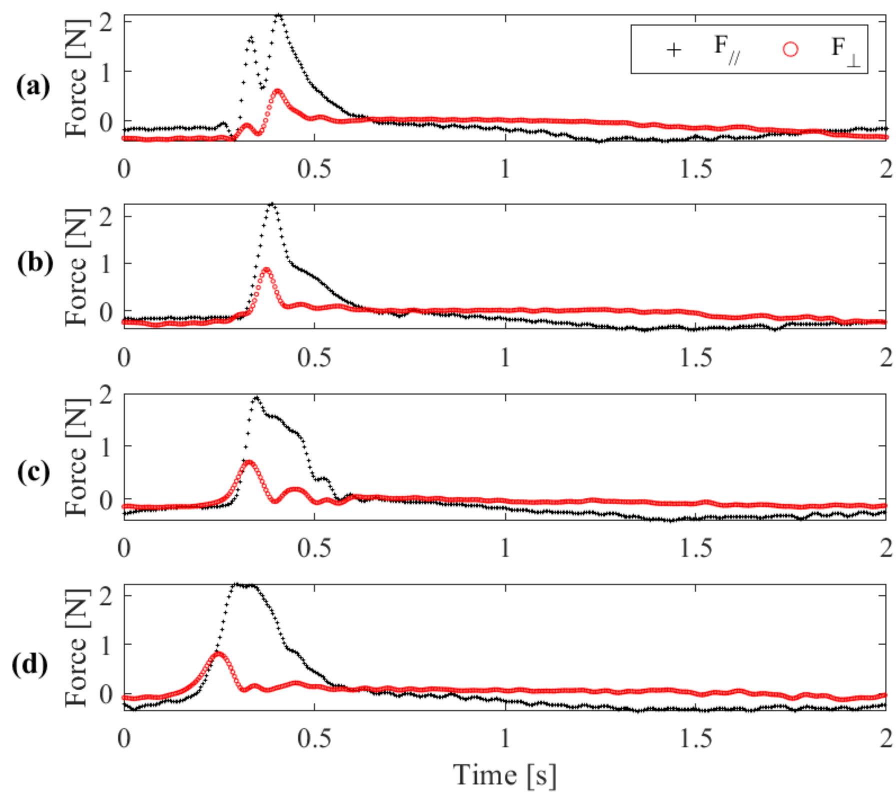

As discussed in Section 4, the positive peak of $F_{//}$ occurs when the local flow reverses due to the arrival of main run-up flow, so $F_{//}$ at this moment is well correlated with $a_{//}$ and thus is akin to the inertial force component in Morrison equation. A negative $F_{//}$ occurs during the run-down phase, when $u_{//}$ is downslope but $a_{//}$ is almost zero, so it is dominated by drag force. These observations suggest that Morrison equation can be used. The buoyancy acting on an armour unit may not be fully captured by the Morison equation. Since an armour unit, if located at or above the still water line, can be partially submerged or emerged, so it does not receive a constant buoyancy, which is only applied to a constantly-submerged armour unit. In view of this, a pressure gradient force, which is proportional to the product of local pressure gradient and density of the mixed media, is added to the Morison equation. As will be introduced later, a 'lift' force is also introduced as a component of $F_{\perp}$.

The drag force is given by

$$\overrightarrow{F_D} = (F_{D//}, F_{D\perp}) = \frac{1}{2} C_D \rho_m |U| (A_{//} U_{//}, A_{\perp} U_{\perp}) \tag{10}$$

where C_D is a drag coefficient to be calibrated; $A_{//}$ and $A_{\perp}$ are the projected areas of the armour unit in the slope-parallel and slope-normal directions; $|U|$, $U_{//}$ and $U_{\perp}$ are the magnitude and the two components of the predicted velocity at the centroid of the armour unit, respectively; and ρ_m is the density of the fluid around the armour unit, which is given by

$$\rho_m = \alpha_1 \rho_w \tag{11}$$

The inertial force is given by:

$$\overrightarrow{F_I} = (F_{I//}, F_{I\perp}) = \rho_m \frac{V}{D_{n50}^2} (C_{I//} A_{//} a_{//}, C_{I\perp} A_{\perp} a_{\perp}) \tag{12}$$

where $C_{I//}$ and $C_{I\perp}$ are inertial coefficients to be calibrated; V is the volume of the armour unit and $a_{//}$ and $a_{\perp}$ are the two components of predicted flow acceleration at the armour unit's centroid, respectively. Note that we assume that $F_{I//}$ and $F_{I\perp}$ in Eq. (12) depend on the cuboid shape, so by including $A_{//}/D_{n50}^2$ and $A_{\perp}/D_{n50}^2$ in the definition.

For the cuboid used in this study, the nominal diameter is given by

$$D_{n50} = (w_m \times h_m \times l_m)^{(1/3)} \tag{13}$$

The volume of cuboid V is calculated using,

$$V = w_m \times h_m \times l_m \tag{14}$$

The projected areas are given by

$$A_{//} = (l_m w_m, h_m w_m) \cdot (\frac{1}{\sqrt{1+m^2}}, \frac{m}{\sqrt{1+m^2}}) \tag{15}$$

and

$$A_{\perp} = (l_m w_m, h_m w_m) \cdot (\frac{m}{\sqrt{1+m^2}}, \frac{1}{\sqrt{1+m^2}}) \tag{16}$$

where m is the revetment slope ($m = 3$ in the present study).

The pressure gradient force is given by

$$\overrightarrow{F_P} = (F_{P//}, F_{P\perp}) = -V(\frac{\partial p}{\partial \xi}, \frac{\partial p}{\partial \tau}) \tag{17}$$

where p is the pressure predicted at the centroid of the armour unit, and ξ and τ denote the parallel and normal directions.

By assembling all components in the parallel direction, $F_{//}$ can be written as

$$F_{//} = F_{D//} + F_{I//} + F_{P//} \tag{18}$$

In the normal direction, we found that the three terms together cannot give a negative $F_\perp$ during the run-down stage ($t = 0$ to 0.2 s in Fig. 9). Thus, we decided to include a 'lift force F_L', which is given by

$$F_L = \frac{1}{2} C_L \rho_m A_{//} |U| U_{//} \tag{19}$$

where C_L is a lift coefficient to be calibrated. We acknowledge that this term has little physical meaning, and is merely for making the predictor better fits the measurement. However, we do note that some other researchers also found that lift force coefficient for a rock unit on the slope of a breakwater can be negative (e.g. Tørum, 1994). Note that it does not affect the prediction of peak value of $F_\perp$, since at that moment $U_{//}$ is almost zero. With this additional term, $F_\perp$ can be written as

$$F_\perp = F_{D\perp} + F_{I\perp} + F_{P\perp} + F_L \tag{20}$$

The choice of Morison equation as the template for developing the force predictor requires some discussions. The Morison equation is for predicting the in-line force of a body submerged in an oscillatory flow, but here it is applied for predicting a 2D force on a body that may be partially submerged. The typical application of Morison equation, such as a cylinder in an oscillatory flow, assumes an undisturbed far-field flow around the body, but here the flow around an armour unit always varies drastically in the slope-normal direction. This is because there is both free flow above the armour layer and porous media flow below the armour layer. Thus, using the velocity predicted at the centroid of the armour unit as model inputs is fundamentally different from using the uniform far-field flow as model inputs in typical applications of the Morison equation. It can be argued that we borrowed the format of the Morison equation, which is inspired by the observed correlations between flow and force. As such, the coefficients to be calibrated are not expected to agree with those for typical applications of Morison equation. This is why we introduced two inertial coefficients in the two directions. Note that only one drag coefficient is introduced because we assume that the drag force to be in line with the instantaneous velocity. Also, no calibration parameter is introduced in the pressure-gradient force (Eq. (17)), because we want this term to be able to give the buoyancy for a unit partially submerged in the water.

5.2. Model calibration

In order to calibrate the parameters in Eqs. (10), (12) and (19) (C_D, $C_{I//}$, $C_{I\perp}$ and C_L), we used the velocity and acceleration at the centroid of the cuboid as characteristic flow quantities around the whole cuboid. We also used the pressure gradient to calculate pressure gradient force. Fig. 14 shows an example ($h0.686H0.10T2.0$, $I_r = 2.76$).

The calibration process is as follows.

First, we subtract the pressure gradient force, $F_{P//}$ from the measurement. Note that the definition of $F_{P//}$ and $F_{P\perp}$ in Eq. (17) include the hydrostatic pressure gradient, while buoyancy was subtracted from the measured force (as stated at the end of section 2), so here the 'dynamic' pressure force is calcuated with the pressure gradient without the hydrostatic components.

Second, for $F_{//}$ in Fig. 14a, the positive peak occurs when the parallel velocity changes from negative to positive, i.e., the parallel flow velocity is about 0 when $F_{//}$ reaches the positive peak as presented in Section 4.1. Therefore, the positive peak of $F_{//}$ (indicated by the left red dashed line in

Fig. 14a) is given by the sum of pressure gradient force $F_{P//}$ and inertial force $F_{I//}$ as drag force $F_{D//}$ is about 0 at this moment. This allows us to calculate $C_{I//}$ in Eq. (12).

Third, the $F_{//}$ during the run-down stage (indicated by the right red lines in Fig. 14a) is negative and the dominant contributor of this negative force is drag force $F_{D//}$. We can subtract $F_{I//}$ and $F_{P//}$ from the measured $F_{//}$ during the run-down stage to give $F_{D//}$, which is then used to calculate C_D in Eq. (10).

Fourth, both the pressure gradient force, $F_{P\perp}$, and the drag force, $F_{D\perp}$, which is calculated using the obtained C_D are subtracted from the measured $F_{\perp}$. In the remaining $F_{\perp}$, the positive peak is dominated by the inertial force, $F_{I\perp}$, so we can calculate $C_{I\perp}$ using this positive peak (the left red dashed line in Fig. 14b-1). At the moment indicated by right red line, the sum of $F_{D\perp}$, $F_{I\perp}$ and $F_{P\perp}$ is larger than the measured $F_{\perp}$. Therefore, the only source of negative force around this moment comes from F_L and it can be used to make the tails of simulated force time history better match the measurement. C_L can be obtained by fitting Eq. (19) to ($F_{\perp}$-$F_{D\perp}$-$F_{I\perp}$-$F_{P\perp}$). The model is successfully calibrated after these steps. The same calibration process is applied to all the cases in this study.

Comparing the fitted coefficients for all cases, it is found that the coefficients for inertial force, i.e., $C_{I//}$ and $C_{I\perp}$, have a significant variation. As shown in Figs. 15a-1 and a-2, both $C_{I//}$, $C_{I\perp}$ for Group 1 cases clearly increase with H_0T_0. As H_0T_0 increases from 40 to 110, $C_{I//}$ increases from 4 to 20, while $C_{I\perp}$ increases from almost zero to 10. As introduced before, H_0T_0 is a controlling parameter of the positive peaks of impact force, which is

Figure 14: An example of the calibration of coefficients in the force predictor (h0.686H0.10T2.0, $I_r = 2.76$): (a) $F_{//}$; (b) $F_{\perp}$. The left red dashed line represents the moment of peak $F_{//}$ and the right dashed line highlights a moment in the run-down stage.

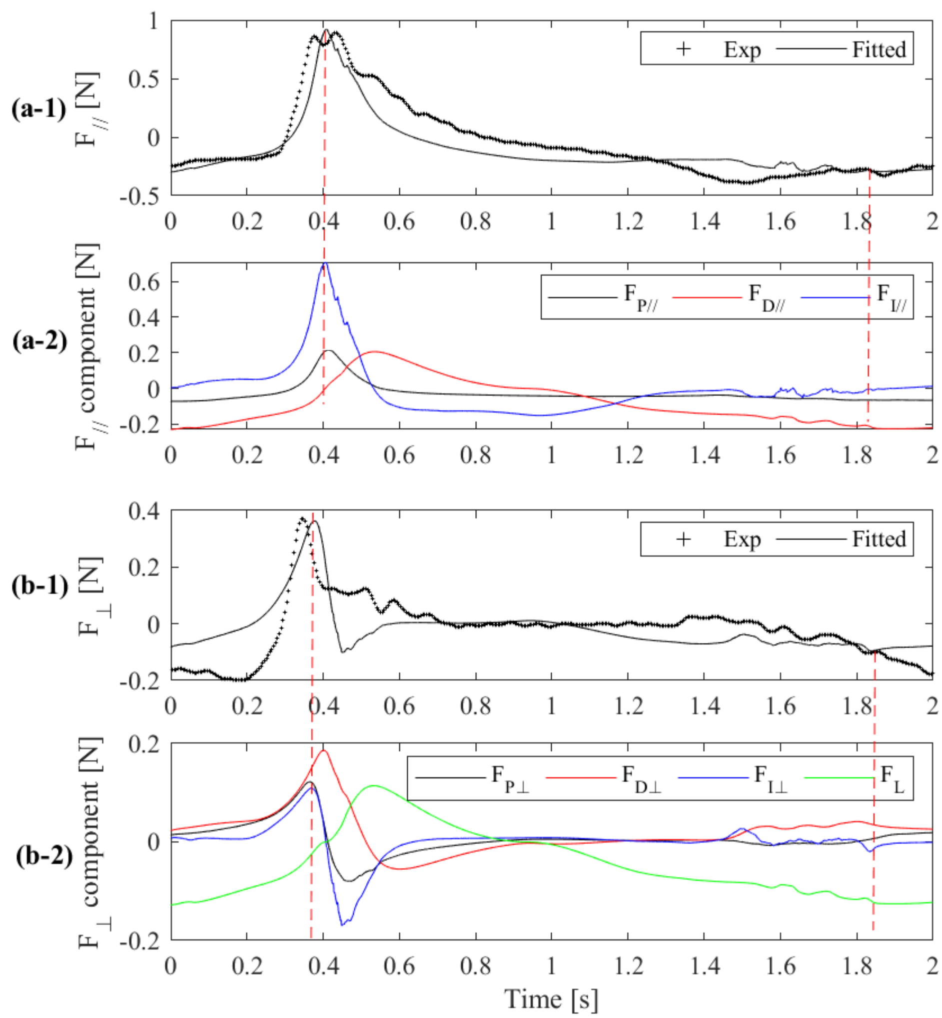

dominated by the inertial force, so this parameter should significantly influence the inertial cofficients. For Group 2 cases, which have similar H_0T_0, we also fitted the coefficients and present $C_{I//}$ and $C_{I\perp}$ in Figs. 15b-1 and b-2. We can see that both $C_{I//}$ and $C_{I\perp}$ increase with h_l/D_{n50}, i.e., as h_l/D_{n50} increass from 0.31 to 2.2, $C_{I//}$ increases from 5 to 22, and $C_{I\perp}$ increases from 4 to 15. It is interesting to see such a big variation of $C_{I//}$ and $C_{I\perp}$ within a small range of h_l/D_{n50}. Despite the large variability, the trend of variations of inertial coefficients are clearly suggested by the data clouds. However, the amount of data we have is insufficient to calibrate prediction formulae for the coefficients and more work is needed in the future study to produce a large enough dataset for the formulae.

For all the cases, the correlations of C_D and C_L with H_0T_0 seem not very obvious. Generally, C_D and C_L are within the range of 12∼20 and 3∼12, respectively, so we simply take $C_D = 16$ and $C_L = 8$. This is acceptable as C_D and C_L do not affect the prediction of the dominant positive peaks significantly.

The obtained $C_{I//}$, $C_{I\perp}$, C_D and C_L are larger than the values in other studies (e.g. Hofland, 2005). This is because the reference velocities and accelerations are the volume-averaged values inside the porous media, which are much smaller than those outside the porous media.

Figs. 16a and b show the comparison between the calculated force using teh force predictor and the best-fit model coefficients and the measured forces for two Group 1 cases. For both $F_{//}$ and $F_{\perp}$, the predicted time series reasonably follow the measurements. For $F_{//}$, the part of the time series around the positive peak is well captured, which is partly because the VARANS

Figure 15: Plot of calibrated: (a-1) $C_{I//}$ and (a-2) $C_{I\perp}$ against H_0T_0 for Group 1 cases; (b-1) $C_{I//}$ and (b-2) $C_{I\perp}$ against h_l/D_{n50} for Group 2 cases. In each sub-figure, 2nd-order polynomial fits (the red solid line) are introduced to depict the trend.

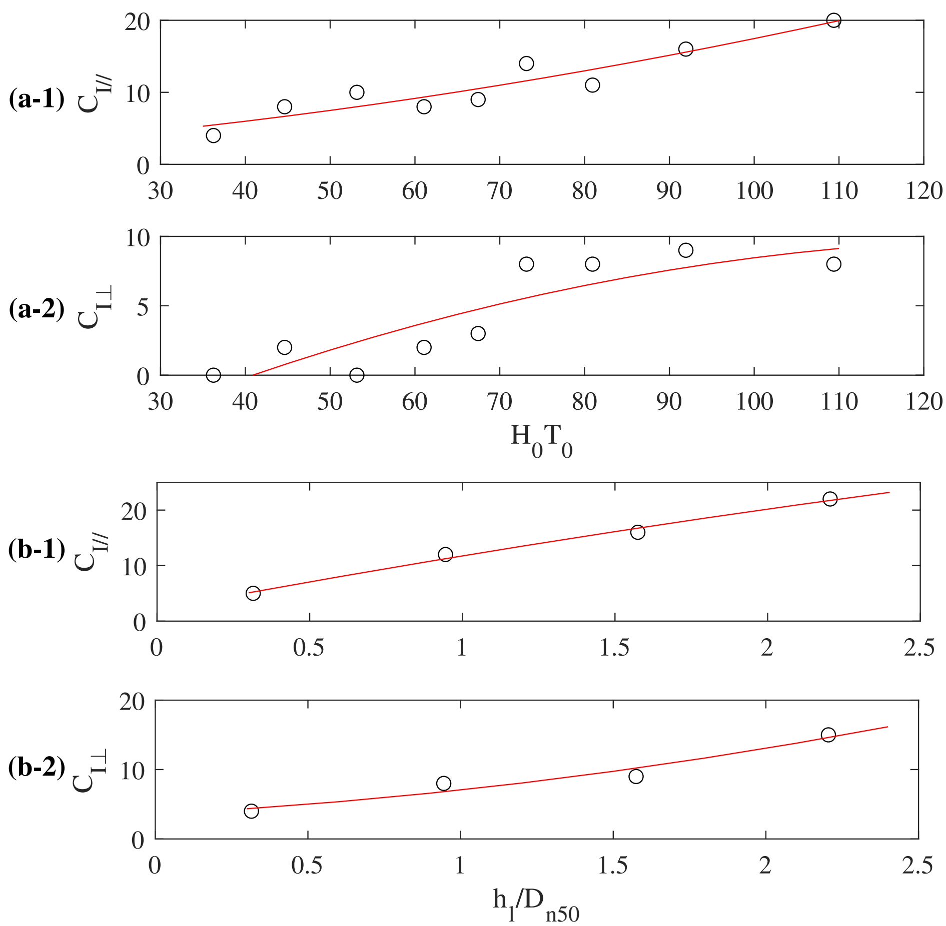

model accurately predicts the behavior of the front of the run-up flow. The 'tail' part of $F_{//}$'s time series (e.g., around $t = 1$ s in Fig. 16a-1) is also well predicted, which justifies the assumption of drag-dominant condition during the run-down stage. The agreement for $F_{\perp}$ is generally worse than that for $F_{//}$. This is partly becasuse $F_{\perp}$ is much smaller than $F_{//}$. Since our model calibration ensures that the positive peak of $F_{\perp}$ is well captured, the prediced postivie peaks indeed agree well with the measurements. Shortly after the positive peak, e.g., around $t = 0.3$ s in both Figs. 16a-2 and b-2, there is a sudden dip of $F_{\perp}$, which is due to a large negative $a_{\perp}$. In fact, we have tried many other ways to parameterize the predictor of $F_{\perp}$, and we found that this dip cannot be explained and described in an easy way. Perhaps some detailed physical processes, such as the release of entrained air bubbles carried by the run-up flow, is related to this dip.

5.3. Shape effect

The two tests in Group 3 (C2 and C3) are not involved in model calibration and they have the same initial submergence and flow condition as test A8 (h0.686H0.137T2.0) in Group 1. Note that D_{n50} of the cuboids for the three cases in Group 3 tests (C1 to C3) are also similar and the only difference among the cases is the cuboid shape which results in different projected areas ($A_{//}$ and $A_{\perp}$). Table 4 summarizes these geometric parameters. Since D_{n50}, initial submergence and wave conditions of the three cases are the same or very similar, $H_0 T_0$ and h_l/D_{n50} are therefore very close, so the model coefficients are expected to be about the same (i.e., $C_{I//} = 16$, $C_{I\perp} = 9$, C_D =16, $C_L = 8$). Thus, here we use the best-fit model coefficients from C1 to predict the wave-induced force for C2 and C3. The model-data com-

Figure 16: Comparisons of the predicted and measured forces for the cases: (a) $h0.686H0.15T1.2$; (b) $h0.686H0.18T2.0$

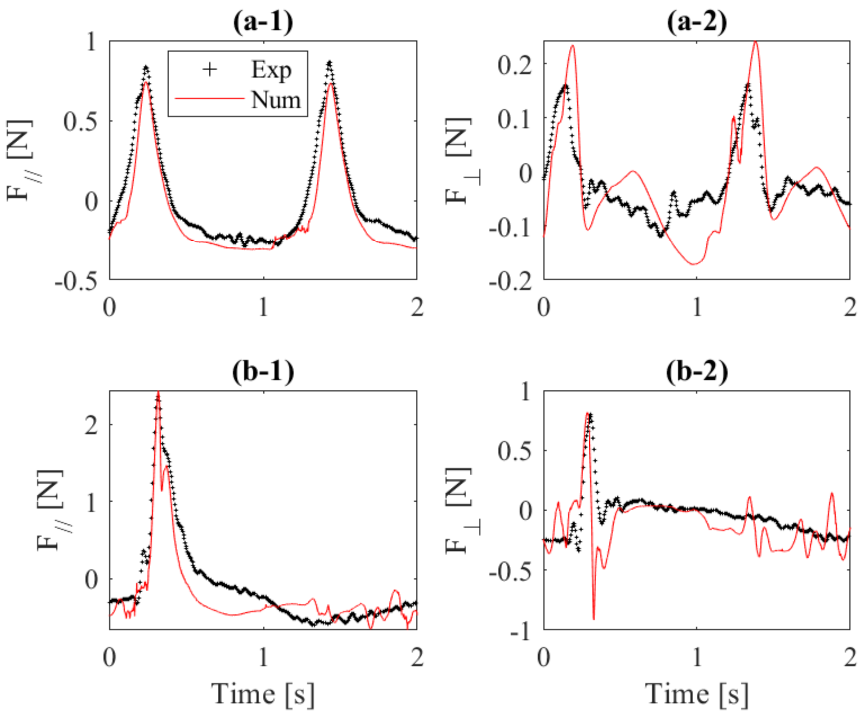

Table 4: Geometric parameters for tests C1 to C3

Test ID	D_{n50} [m]	$A_{//}$ [m^2]	$A_{\perp}$ [m^2]
C1	0.0317	0.00126	0.00177
C2	0.0311	0.00089	0.00114
C3	0.0311	0.00174	0.00142

parisons are presented in Fig. 17. Overall speaking, the agreement is similar to that of the calibrated tests shown in Fig. 16. The $A_{//}$ of test C3 is about twice of $A_{//}$ of test C2, so according to Eq. (12), the positive peak of $F_{//}$ in test C3 should be much larger than that in test C2. This is in agreement with the experiment results, i.e., the measured values are 3.1 N for C1 (see Fig. 17b-1) and 2.2 N for C2 (see Fig. 17a-1). The $A_{\perp}$ of these two tests, however, have similar values, so $F_{\perp}$ have similar magnitude (Fig. 17a-2 vs Fig. 17b-2). This shows that projected area introduced in the force predictor can partially account for the shape effect. However, the angularity of the armour layer unit is another aspect of shape effect, which is unfortunately not included here. More tests with other unit shapes are required in the future study.

6. Conclusion

The present study aims to explore if a Morison-type equation can be used to 'translate' flow predictions from VARANS-based numerical models to wave-induced force on a single armour unit located on a sloped revetment. To this end, we combined wave flume experiments and numerical simulations. In the flume experiments, a cuboid, as an idealization of rock unit, was placed inside the armour layer of a model revetment. It was connected to a load

Figure 17: Comparisons of the predicted and measured forces for: (a) $h0.686H0.15T2.0$ with $2\times5\times3$ cm cuboid (see Fig. 3b and C2 test); (b) $h0.686H0.15T2.0$ with $5\times2\times3$ cm cuboid (see Fig. 3c and C3 test).

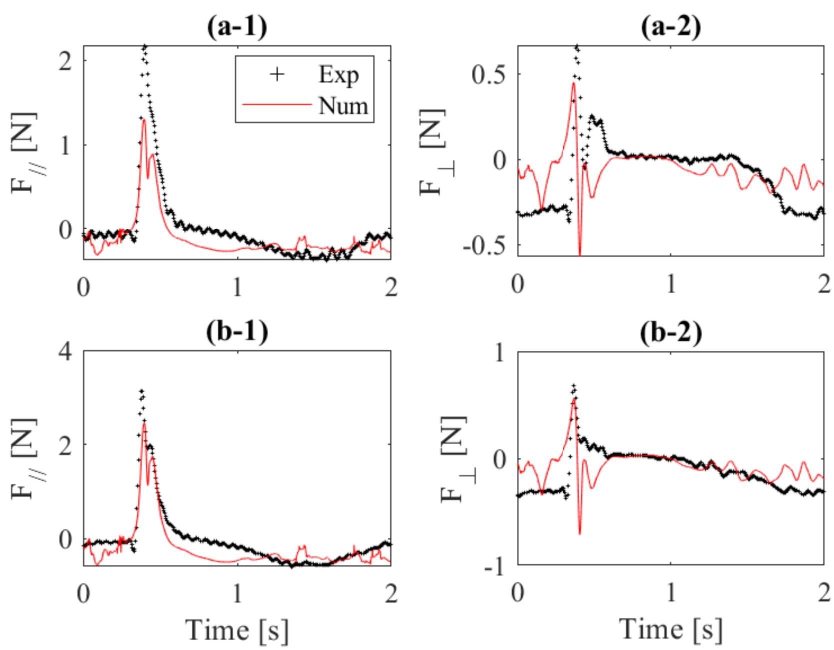

cell fixed above the revetment, allowing direct measurements of impact force. Wave gauges and pressure sensors were also deployed to measure free-surface elevations in the flume and pore pressures within the porous revetment, respectively, which were used for model validation. A high-speed camera was used to record the flow process, and the recording was synchronized with other measurements. 2-dimensional numerical simulations of the wave flume tests were conducted using an OpenFOAM solver, olaFlow, which solves the two phase VARANS equations. A convergence test was performed to ensure that the resolution of the structured grid is sufficiently fine. Comparisons with our measurements showed that the model can accurately predict the surface elevation at the toe of the structure and the pore pressures within the structure.

We focus on armour units located within a narrow belt below the still water line, which is the most vulnerable region for damage. Three group of test conditions were involved in this study. Group 1 tests have the same initial submergence of the cuboid but different wave conditions, which covers a wide range of Iribarren number, I_r, and dynamic stability number H_0T_0. Group 2 tests have the same wave condition but different initial submergence (h_l/D_{n50} from 0.31 to 2.2). In group 3, the shape of the cuboid is changed, while flow condition and initial submergence are kept unchanged.

By synchronizing the force measurements and the prediction of flow field, some key correlations between flow and wave loading on a single armour unit are identified. First, the positive peak of slope-parallel force component, $F_{//}$, occurs when the arrival of the run-up flow suddenly reverses the flow around an armour unit from run-down to run-up, so it is correlated with the slope-parallel acceleration. The positive peak of slope-normal force component, $F_{\perp}$, occurs slightly before the positive peak of $F_{//}$. It is associated with an outward seepage flow, which is created when inside the porous revetment an offshore flow driven by a falling internal water table meets an onshore flow driven by the arriving wave. During the run-down stage, a thin layer of down-slope surface flow covers an armour unit, so the $F_{//}$ is correlated with the instantaneous bottom-parallel velocity.

Based on these observed correlations, a force predictor, which consists of an inertial force, a drag force, a pressure-gradient force and a lift force (only for $F_{\perp}$), is proposed. The predictor follows the classic Morison equation, i.e., the inertial force is scaled with flow acceleration and the drag force is given by a quadratic law. Its input flow parameters are from the predicted porous media flow at the centroid of the armour unit, while in typical applications of Morison equation the far-field flow is usually taken as the input. As such, the model coefficients are not expected to take the values used in other typical applications of Morison equation, and therefore are calibrated using our own data. After fitting the predictor to the measurments, it is found that the proposed force predictor can generally approximate the temporal variation of the impact force in the bottom-parallel direction. In the bottom-normal direction, the predictor can approximate the peak values, but not all temporal variations can be perfectly captured. It is found that the inertial coefficients vary substantially with H_0T_0 and h_l/D_{n50}, while the drag and lift coefficients have much less variability. Although the inertial coefficient varies with the submergence h_l/D_{n50}, the peak force does not change significantly with h_l/D_{n50}. Due to the lack of data, we leave calibrating empirical formulae for inertial coefficients to the future. The shape of the amour unit is considered by introducing projected areas in the force predictor. By applying the predictor using the same set of model coefficients to three tests in group 3, among which the only difference is the shape of the cuboid, it was found that this set-up indeed can capture the shape effect to a large extent.

Overall speaking, this study has demonstrated the feasibility of developing a Morison-type equation that can translate a VARANS-based model's prediction of porous-media flow in the armour layer into the wave-induced force on the armour unit. It is found that the inertial force is the dominant force, but the inertial coefficients can have significant variations with the dynamic stability number H_0T_0 and the submergence h_l/D_{n50}. Our dataset shows that the inertial coefficients increases with both H_0T_0 and h_l/D_{n50}, but a much larger dataset is required for calibrating emprical formulae that describe the variations. To eventually develop a force predictor that can be used in engineering practices, a large amount of research work is required to fully achieve our ultimate target, including tests of irregular wave, test of larger ranges of H_0T_0 and h_l/D_{n50} and rock units with various shapes.

Acknowledgments

The Department of Civil and Environmental Engineering in National University of Singapore is acknowledged for allowing us to use the hydraulic laboratory. National Supercomputing Center Singapore (NSCC) is acknowledged for providing the computing facilities for the present study.

References

Altomare, C., Crespo, A., Rogers, B., Dominguez, J., Gironella, X., Gómez-Gesteira, M., 2014. Numerical modelling of armour block sea breakwater with smoothed particle hydrodynamics. Computers & Structures 130, 34–45. doi:https://doi.org/10.1016/j.compstruc.2013.10.011.

Anastasaki, E., Latham, J.P., Xiang, J., 2015. Numerical modelling of armour layers with reference to core-loc units and their placement acceptance criteria. Ocean Engineering 104, 204–218. doi:https://doi.org/10.1016/j.oceaneng.2015.05.010.

CIRIA, d., 2007. CIRIA, CUR, CETMEF, (2007), The Rock Manual. The use of rock in hydraulic engineering (2nd edition). C683, CIRIA, London.

Cornett, A.M., 1995. A study of wave-induced forcing and damage of rock armour on rubble-mound breakwaters. Ph.D. thesis. University of British Columbia.

Díaz-Carrasco, P., Eldrup, M.R., Lykke Andersen, T., 2021. Advance in wave reflection estimation for rubble mound breakwaters: The importance of the relative water depth. Coastal Engineering 168, 103921. doi:https://doi.org/10.1016/j.coastaleng.2021.103921.

del Jesus, M., Lara, J.L., Losada, I.J., 2012. Three-dimensional interaction of waves and porous coastal structures: Part i: Numerical model formulation. Coastal Engineering 64, 57 – 72.

DMC, 2003. General xbloc specifications, xbloc technical guidelines. Delta Marine Consultants, Gouda URL: `www.xbloc.com`.

Etemad-Shahidi, A., Bali, M., van Gent, M.R., 2021. On the toe stability of rubble mound structures. Coastal Engineering 164, 103835. doi:https://doi.org/10.1016/j.coastaleng.2020.103835.

Gerding, E., 1993. Toe structure stability of rubble mound breakwaters. Master's thesis. Delft University of Technology. URL: `http://repository.tudelft.nl/`.

Goda, Y., Suzuki, Y., 1976. Estimation of incident and reflected waves in random wave experiments. Proceedings of 15th International Conference on Coastal Engineering , 828–845.

Herrera, M.P., Gómez-Martín, M.E., Medina, J.R., 2017. Hydraulic stability of rock armors in breaking wave conditions. Coastal Engineering 127, 55–67. doi:https://doi.org/10.1016/j.coastaleng.2017.06.010.

Higuera, P., 2015. Aplicación de la dinámica de fluidos computacional a la acción del oleaje sobre estructuras. Application of computational fluid dynamics to wave action on structures. Ph.D. thesis. University of Cantabria.

Higuera, P., Lara, J.L., Losada, I.J., 2014. Three-dimensional interaction of waves and porous coastal structures using openfoam®. part i: Formulation and validation. Coastal Engineering 83, 243–258.

Hofland, B., 2005. Rock and roll: Turbulence-induced damage to granular bed protections. Ph.D. thesis. Delft University of Technology. URL: `www.library.tudelft.nl`.

Hudson, R., Jackson, R., 1953. Stability of rubble-mound breakwaters. Technical Memorandum 2-365; Waterways Experiment Station, CERC: Vicksburg, MS, USA .

Jacobsen, N.G., Fuhrman, D.R., Fredsøe, J., 2012. A wave generation toolbox for the open-source cfd library: Openfoam®. International Journal for Numerical Methods in Fluids 70, 1073–1088.

Jensen, B., Jacobsen, N.G., Christensen, E.D., 2014. Investigations on the porous media equations and resistance coefficients for coastal structures. Coastal Engineering 84, 56 – 72.

Kobayashi, N., Otta, A.K., 1987. Hydraulic stability analysis of armor units. Journal of Waterway, Port, Coastal, and Ocean Engineering 113, 171–186. doi:10.1061/(ASCE)0733-950X(1987)113:2(171).

Larsen, B.E., Fuhrman, D.R., 2018. On the over-production of turbulence beneath surface waves in reynolds-averaged navier–stokes models. Journal of Fluid Mechanics 853, 419–460. doi:10.1017/jfm.2018.577.

Latham, J.P., Mindel, J., Xiang, J., Guises, R., Garcia, X., Pain, C., Gorman, G., Piggott, M., Munjiza, A., 2009. Coupled femdem/fluids for coastal engineers with special reference to armour stability and breakage. Geomechanics and Geoengineering 4, 39–53. doi:10.1080/17486020902767362.

Losada, M., Medina, R., Alejo, M., 1988. Wave forces on armour blocks. Proceedings of the 21st International Conference on Coastal Engineering , 2479–2488.

Losada, M.A., Gimenez-Curto, L.A., 1979. The joint effect of the wave height and period on the stability of rubble mound breakwaters using iribarren's number. Coastal Engineering 3, 77–96. doi:https://doi.org/10.1016/0378-3839(79)90011-5.

van der Meer, J.W., 1988. 5. Stability of rubble mound revetments and breakwaters under random wave attack. pp. 141–154. URL: https://www.icevirtuallibrary.com/doi/abs/10.1680/dib.02661.0009, doi:10.1680/dib.02661.0009.

Moghim, M., Tørum, A., 2012. Wave induced loading of the reshaping rubble mound breakwaters. Applied Ocean Research 37, 90–97. doi:https://doi.org/10.1016/j.apor.2012.04.001.

PIANC, 2003. State-of-the-art of designing and constructing berm breakwaters. Report of MarCom WG40, PIANC, Brussels .

Pramono, W.T., 1997. Wave forces on cubical armour units on submerged and low-crested breakwaters. Ph.D. thesis. University of Windsor. URL: https://scholar.uwindsor.ca/etd/4550/.

Ren, B., Jin, Z., Gao, R., xue Wang, Y., lin Xu, Z., 2014. Sph-dem modeling of the hydraulic stability of 2d blocks on a slope. Journal of Waterway, Port, Coastal, and Ocean Engineering 140, 04014022. doi:10.1061/(ASCE)WW.1943-5460.0000247.

Sarfaraz, M., Pak, A., 2017. An integrated sph-polyhedral dem algorithm to investigate hydraulic stability of rock and concrete blocks: Application to cubic armours in breakwaters. Engineering Analysis with Boundary Elements 84, 1–18. doi:https://doi.org/10.1016/j.enganabound.2017.08.002.

Sarfaraz, M., Pak, A., 2018. Numerical investigation of the stability of armour units in low-crested breakwaters using combined sph–polyhedral dem method. Journal of Fluids and Structures 81, 14–35. doi:https://doi.org/10.1016/j.jfluidstructs.2018.04.016.

Tirindelli, M., Lamberti, A., 2004. Wave action on rubble mound breakwater: the problem of scale effects. Delos report D52. URL: `http://resolver.tudelft.nl/uuid:379ac067-9986-4461-9160-70c30e5e737a`.

Tørum, A., 1994. Wave induced forces on armor unit on berm breakwaters. Journal of Waterway, Port, Coastal, and Ocean Engineering 120, 251–268.

Van der Meer, J.W., 1987. Stability of breakwater armour layers — design formulae. Coastal Engineering 11, 219–239. doi:https://doi.org/10.1016/0378-3839(87)90013-5.

van Gent, M.R., 2013. Rock stability of rubble mound breakwaters with a berm. Coastal Engineering 78, 35–45. doi:https://doi.org/10.1016/j.coastaleng.2013.03.003.

van Gent, M.R., van der Werf, I.M., 2014. Rock toe stability of rubble mound breakwaters. Coastal Engineering 83, 166–176. doi:https://doi.org/10.1016/j.coastaleng.2013.10.012.

Xiang, J., Latham, J., Higuera, P., Via-Estrem, L., Eden, D., Douglas, S., Simplean, A., Nistor, I., Cornett, A., 2019. A fast and effective wave proxy approach for wave-structure interaction in rubble mound structures. Coastal structures , 702–711.

Yamini, O., Mousavi, S., Kavianpour, M., 2019. Experimental investigation of using geo-textile filter layer in articulated concrete block mattress revetment on coastal embankment. Journal of Ocean Engineering and Marine Energy 5, 119–133. doi:https://doi.org/10.1007/s40722-019-00133-y.

Yamini, O.A., Kavianpour, M.R., Mousavi, S.H., 2018. Wave run-up and rundown on acb mats under granular and geotextile filters' condition. Marine Georesources & Geotechnology 36, 895–906. doi:10.1080/1064119X.2017.1397068.

Nomenclature

α one of the parameters of the porous media. Unit: -

α_1 the volume of fluid (VOF). Unit: -

β one of the parameters of the porous media. Unit: -

Δx grid dimension in x direction. Unit: m

Δz grid dimension in z direction. Unit: m

μ the dynamic molecular viscosity. Unit: $kg/(ms)$

μ_t the dynamic turbulent viscosity. Unit: $kg/(ms)$

ρ the fluid density. Unit: kg/m^3

ρ_a the air density. Unit: kg/m^3

ρ_m $=\alpha_1 \rho_w$. Unit: kg/m^3

ρ_w the water density. Unit: kg/m^3

τ the direction normal to the slope. Unit: -

ξ the direction parallel to the slope. Unit: -

A coefficient. Unit: -

$A_{//}$ force area parallel to the slope. Unit: m^2

$a_{//}$ acceleration parallel to the slope. Unit: m/s^2

$A_{\perp}$ force area perpendicular to the slope. Unit: m^2

$a_{\perp}$ acceleration perpendicular to the slope. Unit: m/s^2

B coefficient. Unit: -

c coefficient, $c = 0.34$. Unit: -

C_D drag coefficient. Unit: -

C_I inertia coefficient. Unit: -

C_L lift coefficient. Unit: -

$C_{I//}$ inertia coefficient for parallel force component. Unit: -

$C_{I\perp}$ inertia coefficient for perpendicular force component. Unit: -

D_{n50} median nominal diameter of the rock. Unit: m

F_r Froude number, $F_r = U/\sqrt{gD_{n50}}$, here $U = \sqrt{gH}$. Unit: -

$F_{//}$ the force parallel to the slope. Unit: $kg \cdot m/s^2$

$F_{\perp}$ the force perpendicular to the slope. Unit: $kg \cdot m/s^2$

$F_{D//}$ the darg force parallel to the slope. Unit: $kg \cdot m/s^2$

$F_{D\perp}$ the drag force perpendicular to the slope. Unit: $kg \cdot m/s^2$

$F_{I//}$ the inertial force parallel to the slope. Unit: $kg \cdot m/s^2$

$F_{I\perp}$ the inertial force perpendicular to the slope. Unit: $kg \cdot m/s^2$

$F_{P//}$ the pressure difference force parallel to the slope. Unit: $kg \cdot m/s^2$

$F_{P\perp}$ the pressure difference force perpendicular to the slope. Unit: $kg{\cdot}m/s^2$

g the gravitational acceleration. Unit: m/s^2

H the wave height. Unit: m

h the water depth. Unit: m

H_0 the static stability number, $H_0 = H_s/(\Delta D_{n50})$. Unit: -

H_0T_0 the dynamic stability number, $H_0T_0 = H_0 \cdot T_0$. Unit: -

h_l the local water depth above the cuboid. Unit: m

h_m the height of the cuboid. Unit: m

I_r Iribarren number, $I_r = \tan\beta/\sqrt{H/L_0}$. Unit: -

KC the Keulegan-Carpenter number, $KC = U_M T/(nD_{n50})$. Unit: -

L_0 deep water wavelength, $L_0 = gT^2/2/\pi$. Unit: m

l_m the length of the cuboid. Unit: m

m the revetment slope. Unit: -

n the porosity. Unit: -

N_s an index to quantify stability condition of a structure. Unit: -

p the pressure. Unit: $kg/(ms^2)$

p^* the pseudo-dynamic pressure. Unit: $kg/(ms^2)$

R_e Reynolds number, $R_e = \sqrt{gH}D_{n50}/\nu$ and ν is the kinematic viscosity. Unit: -

T the wave period of regular waves. Unit: s

t time. Unit: s

T_0 the wave period factor, $T_0 = T_m(g/D_{n50})^{0.5}$. Unit: -

U the resultant velocity of $U_{//}$ and $U_{\perp}$. Unit: m/s

u^r the relative velocity between fluid and air. Unit: m/s

u_i the volume-averaged velocity in Cartesian coordinates. Unit: m/s

u_j the volume-averaged velocity in Cartesian coordinates. Unit: m/s

U_M the maximum oscillatory velocity. Unit: m/s

$U_{//}$ the velocity parallel to the slope. Unit: m/s

$U_{\perp}$ the velocity perpendicular to the slope. Unit: m/s

V the volume of the cuboid. Unit: m^3

w_m the width of the cuboid. Unit: m

x the horizontal coordinate. Unit: m

x_i the Cartesian coordinate. Unit: m

y the vertical coordinate. Unit: m

y_i the Cartesian coordinate. Unit: m